

COPY
Naval Research Laboratory

Washington, DC 20375-5000



NRL Memorandum Report 6589

AD-A219 513

Stability Regimes in a Rotating Quadrupole Focusing Accelerator

C.M. TANG, P. SPRANGLE, J. KRALL P. SERAFIM* AND F. MAKO**

*Beam Physics Branch
Plasma Physics Division*

**Northeastern University
Boston, MA 02115*

***FM Technologies, Inc.
Alexandria, VA 22304*

March 7, 1990

REC
FILE
MAR 21 1990
D
EC

90 03 20 160

REPORT DOCUMENTATION PAGE				Form Approved OMB No 0704-0188	
1a. REPORT SECURITY CLASSIFICATION UNCLASSIFIED			1b. RESTRICTIVE MARKINGS		
2a. SECURITY CLASSIFICATION AUTHORITY			3. DISTRIBUTION / AVAILABILITY OF REPORT Approved for public release; distribution unlimited.		
2b. DECLASSIFICATION / DOWNGRADING SCHEDULE			5. MONITORING ORGANIZATION REPORT NUMBER(S)		
4. PERFORMING ORGANIZATION REPORT NUMBER(S) NRL Memorandum Report 6589			7a. NAME OF MONITORING ORGANIZATION Naval Surface Warfare Center		
6a. NAME OF PERFORMING ORGANIZATION Naval Research Laboratory		6b. OFFICE SYMBOL (If applicable) Code 4790	7b. ADDRESS (City, State, and ZIP Code) Silver Spring, MD 20903-5000		
6c. ADDRESS (City, State, and ZIP Code) Washington, DC 20375-5000			9. PROCUREMENT INSTRUMENT IDENTIFICATION NUMBER		
8a. NAME OF FUNDING / SPONSORING ORGANIZATION DARPA		8b. OFFICE SYMBOL (If applicable)	10. SOURCE OF FUNDING NUMBERS		
8c. ADDRESS (City, State, and ZIP Code) Arlington, VA 22209			PROGRAM ELEMENT NO 62707E	PROJECT NO 4395.A80	TASK NO WORK UNIT ACCESSION NO DN680-415
11. TITLE (Include Security Classification) Stability Regimes in a Rotating Quadrupole Focusing Accelerator					
12. PERSONAL AUTHOR(S) Tang, C.M., Sprangle, P., Krall, J., Serafim,* P. and Mako,* F.					
13a. TYPE OF REPORT Interim		13b. TIME COVERED FROM _____ TO _____		14. DATE OF REPORT (Year, Month, Day) March 7, 1990	
15. PAGE COUNT 50					
16. SUPPLEMENTARY NOTATION *Northeastern University, Boston, MD 02115 **FM Technologies, Inc., Alexandria, VA 22304					
17. COSATI CODES			18. SUBJECT TERMS (Continue on reverse if necessary and identify by block number)		
FIELD	GROUP	SUB-GROUP	Accelerator Stellarator fields		
			Rotating quadrupole		
19. ABSTRACT (Continue on reverse if necessary and identify by block number) A number of high current accelerator designs utilize strong focusing in the form of helical quadrupole and axial guide fields. We obtain a linear dispersion relation for an electron beam propagating in a cylindrical waveguide subject to helical quadrupole and longitudinal magnetic fields, electromagnetic waveguide modes and image fields. The electromagnetic waveguide modes are expressed in terms of right-hand and left-hand circularly polarized waves. We find that the electron beam centroid, depending on the system parameters, can be i) orbit unstable independent of the waveguide modes, ii) three-wave unstable or iii) fully stable. Analytic expressions for the various stability conditions are obtained in the limit of zero beam current, where the right-hand and left-hand circularly polarized waves decouple. Algebraic expressions for the growth rate in each of the three-wave unstable regimes are presented. The full dispersion relation is solved numerically with results that are in good agreement with both the stability conditions and the growth rate expressions.					
20. DISTRIBUTION / AVAILABILITY OF ABSTRACT <input checked="" type="checkbox"/> UNCLASSIFIED/UNLIMITED <input type="checkbox"/> SAME AS RPT <input type="checkbox"/> DTIC USERS			21. ABSTRACT SECURITY CLASSIFICATION UNCLASSIFIED		
22a. NAME OF RESPONSIBLE INDIVIDUAL C.M. Tang			22b. TELEPHONE (Include Area Code) (202) 767-4148		22c. OFFICE SYMBOL Code 4791

CONTENTS

I. INTRODUCTION	1
II. MODEL	2
III. STABILITY REGIMES AND ANALYTICAL EXPRESSIONS FOR GROWTH RATES	11
IV. NUMERICAL RESULTS	16
V. CONCLUSIONS	20
ACKNOWLEDGEMENTS	21
REFERENCES	22
DISTRIBUTION LIST	43

Accession For	
NTIS AD-1	<input checked="" type="checkbox"/>
DISC CD	<input type="checkbox"/>
Un- JL	<input type="checkbox"/>
By _____	
Distribution/	
Availability Code	
Dist Special	
A-1	



STABILITY REGIMES IN A ROTATING QUADRUPOLE FOCUSING ACCELERATOR

I. INTRODUCTION

A number of recent high current accelerator configurations utilize strong focusing fields. These fields, consisting of a stellarator field (or rotating quadrupole field) and an axial guide field, increase considerably the energy mismatch tolerance of the device and provide confining forces against the beam space charge forces.^{1,2} Two such devices are the modified betatron accelerator³ and the spiral line induction accelerator (SLIA).⁴⁻⁶ The recent addition of strong focusing to the modified betatron at the Naval Research Laboratory has allowed that accelerator to successfully accelerate a 0.5 kA beam to 12 MeV for $\simeq 35,000$ turns in a vacuum chamber with resistive walls.⁷ The SLIA, to be constructed by Pulse Sciences, Inc., will utilize the strong focusing for transport along the curved sections of the beam line between the accelerating cavities.

The use of strong focusing fields has a potential difficulty in that they can lead to various types of beam instabilities.^{8,9} It has been suggested, for example, that the rotating quadrupole field may act like a wiggler field as in the free electron laser.^{8,10} Of interest in this study, however, is the three-wave instability in which the externally imposed rotating quadrupole field interacts with the transverse motion of the beam centroid to excite a transverse-electric (TE) waveguide mode.⁹ Approximate stability conditions for such strong focusing fields have recently been found.¹¹

The purpose of the present study is to obtain detailed analytical conditions for stabilizing the three-wave instability. Here we analyze the dynamics of electromagnetic waveguide modes and the beam modes associated with a relativistic electron beam propagating under the influence of external strong focusing fields. The dispersion relation for such a system is generated in Section II below. In Section III, we show that this dispersion relation, in the limit of zero beam current, gives analytical conditions for the various stability regimes. We find a) two physically distinct three-wave unstable regimes, b) two three-wave stable regimes and c) a regime in which the particle orbits themselves are unstable, irrespective of the electromagnetic waves. The orbit unstable regime is a recovery of an earlier result.^{1,2} In addition, we obtain algebraic expressions for the growth rates in each of the three-wave unstable regimes. This is done with the simplified dispersion relation where the right-hand (RH) and left-hand (LH) circularly polarized waves are decoupled in the

low current regime. These are found to be in general agreement with the approximate expressions given in Ref. 12. Numerical solutions of the dispersion relation are presented in section IV. The analytic expressions of the growth rates and stability boundaries are in good agreement with the numerical results of the dispersion relation.

II. MODEL

In our model the external fields consist of a periodic rotating quadrupole field and a longitudinal magnetic field (see Fig. 1). The electron beam radius is assumed to be small compared to the waveguide radius. In the equilibrium position, the beam is centered along the axis of a circular waveguide and the beam electrons are assumed to be monoenergetic with zero transverse velocity. Perturbing electromagnetic waveguide fields cause the beam centroid to develop a transverse velocity and become displaced off the z-axis. This displacement of the beam centroid amounts to a transverse macroscopic current which, under certain conditions, further excites the electromagnetic field. The displacement of the beam centroid also induces image electric and magnetic fields on the wall of the waveguide. The beam centroid motion, in our model, is governed by the following fields: i) rotating quadrupole field, ii) longitudinal magnetic field, iii) electromagnetic fields, and iv) induced image fields.

Wave equation

Before developing the orbit equations for the beam centroid we first derive the wave equation for the electromagnetic fields. The electromagnetic fields are represented by a vector potential given by,

$$\mathbf{A} = \mathbf{A}_+(x, y, z)e^{-i\omega t} + \mathbf{A}_-(x, y, z)e^{-i\omega t} + c.c., \quad (1)$$

where \mathbf{A}_+ and \mathbf{A}_- are complex amplitudes associated with the right-hand (RH) and left-hand (LH) circularly polarized waves in a cylindrical waveguide. In Eq. (1), ω is the radian frequency and c.c. denotes the complex conjugate.

The wave equation for \mathbf{A} is given by

$$\left(\nabla_{\perp}^2 + \frac{\partial^2}{\partial z^2} - \frac{1}{c^2} \frac{\partial^2}{\partial t^2} \right) \mathbf{A} = -\frac{4\pi}{c} \mathbf{J}, \quad (2)$$

where ∇_{\perp}^2 is the transverse Laplacian, and \mathbf{J} is the macroscopic transverse current associated with the beam centroid. Substituting (1) into (2) and operating on the result with $(\omega/2\pi) \int_0^{2\pi/\omega} dt \exp(i\omega t)$, in order to select the correct frequency dependence, yields

$$L(\mathbf{A}_+ + \mathbf{A}_-) = -\frac{4\pi}{c} \int_0^{2\pi/\omega} \frac{dt}{2\pi/\omega} e^{i\omega t} \mathbf{J}, \quad (3)$$

where $L = \nabla_{\perp}^2 + \partial^2/\partial z^2 + \omega^2/c^2$. To obtain the RH and LH polarized components of the current, we equate the $\hat{\mathbf{e}}_+$ and $\hat{\mathbf{e}}_-$ components of both sides of (3), and find the following wave equation,

$$L(\mathbf{A}_+ + \mathbf{A}_-) \cdot (2\hat{\mathbf{e}}_{\mp}) = -\frac{4\pi}{c} \int_0^{2\pi/\omega} \frac{dt}{2\pi/\omega} (J_{cx} \mp iJ_{cy}) e^{i\omega t}, \quad (4)$$

where $\hat{\mathbf{e}}_{\pm} = (\hat{\mathbf{e}}_x \pm i\hat{\mathbf{e}}_y)/2$ and $\hat{\mathbf{e}}_x$ and $\hat{\mathbf{e}}_y$ denote unit vectors in the x - and y -directions.

The current density associated with the beam centroid motion is

$$\begin{aligned} \mathbf{J}(x, y, z, t) = & -|e|\lambda_b \int_{-\infty}^{\infty} dz_o \left(\frac{\partial x_c(z_o, t)}{\partial t} \hat{\mathbf{e}}_x + \frac{\partial y_c(z_o, t)}{\partial t} \hat{\mathbf{e}}_y \right) \\ & \delta(x - x_c(z_o, t)) \delta(y - y_c(z_o, t)) \delta(z - z_c(z_o, t)), \end{aligned} \quad (5)$$

where $\lambda_b = n_b \pi r_b^2$ is the number of electrons per unit length, n_b is the beam density, r_b is the beam radius, x_c and y_c denote the transverse coordinates of the beam centroid, z_c denotes the axial position of a cross sectional slice of the beam and z_o is the initial position of the slice: $z_c(z_o, t=0) = z_o$. In the small-signal or linear regime x_c and y_c are proportional to the electromagnetic fields and (5) can be written as

$$\begin{aligned} \mathbf{J}_c(x, y, z, t) \simeq & -|e|\lambda_b \delta(x) \delta(y) \\ & \int_{-\infty}^{\infty} dz_o \left(\frac{\partial x_c(z_o, t)}{\partial t} \hat{\mathbf{e}}_x + \frac{\partial y_c(z_o, t)}{\partial t} \hat{\mathbf{e}}_y \right) \delta(z - z_c(z_o, t)), \end{aligned} \quad (6)$$

where v_o is the axial beam velocity. Substituting (6) into (4), we obtain

$$\begin{aligned} L(\mathbf{A}_+ + \mathbf{A}_-) \cdot (2\hat{\mathbf{e}}_{\mp}) = & \frac{4\pi}{c} \nu \delta(x) \delta(y) \int_0^{2\pi/\omega} \frac{dt}{2\pi/\omega} \int_{-\infty}^{\infty} dz_o \\ & \left(\frac{\partial x_c(z_o, t)}{\partial t} \mp i \frac{\partial y_c(z_o, t)}{\partial t} \right) \delta(z - z_o - v_o t) e^{i\omega t}, \end{aligned} \quad (7)$$

where $\nu = (|e|/m_0 c^2) I_b / \beta_0 \simeq I_b [kA] / 17 \beta_0$ is Budker's parameter, I_b is the beam current and $\beta_0 = v_0 / c$. Upon carrying out the time integration in (7) we obtain,

$$L(\mathbf{A}_+ + \mathbf{A}_-) \cdot (2\hat{\mathbf{e}}_{\mp}) = \frac{4\pi}{c} \nu \delta(x) \delta(y) e^{i(\omega/v_0)z} \int_0^{2\pi v_0/\omega} \frac{dz_0}{2\pi v_0/\omega} \frac{\partial}{\partial t} (x_c \mp i y_c) e^{-i\omega z_0/v_0}, \quad (8)$$

where $x_c(z_0, z) = x_c(z_0, t = (z - z_0)/v_0)$ and $y_c(z_0, z) = y_c(z_0, t = (z - z_0)/v_0)$. Since our model is spatially periodic with period $\omega/2\pi$, the limits on the z_0 integral have been changed to 0 to $2\pi/\omega$.

Beam Centroid Orbit

The configuration of the rotating quadrupole and the axial magnetic fields are shown in Fig. 1. The total external magnetic field, \mathbf{B}_{ext} , consists of the rotating quadrupole field and the uniform longitudinal field and is given by $\mathbf{B}_{ext} = (B_{qx}, B_{qy}, B_{zo})$ where

$$\begin{aligned} B_{qx} &= -B_q k_q (x \sin k_q z - y \cos k_q z), \\ B_{qy} &= B_q k_q (x \cos k_q z + y \sin k_q z), \\ B_{zo} &= B_0. \end{aligned} \quad (9a-c)$$

In Eqs. (9a-c), B_0 is the axial magnetic field, B_q is the magnetic field of the quadrupole, $k_q = 2\pi/\lambda_q$ and λ_q is the period of the quadrupole field. The representation for the quadrupole field in Eqs. (9a,b) is valid near the z-axis, i.e., $(x^2 + y^2)^{1/2} < \lambda_q/2\pi$.

In addition to the electromagnetic fields given by (1) and external fields given by (9), we have induced fields due to the displaced beam. These fields are produced by the image charges and currents on the waveguide wall when the beam is displaced off the z-axis. For a circular, perfectly conducting waveguide the induced electric and magnetic fields near the z-axis are

$$\mathbf{E}_{ind} = -2 \frac{m_0 c^2}{|e|} \frac{\nu}{r_g^2} (x_c \hat{\mathbf{e}}_x + y_c \hat{\mathbf{e}}_y), \quad (10a)$$

$$\mathbf{B}_{ind} = 2 \frac{m_0 c^2}{|e|} \frac{\nu}{r_g^2} \beta_0 (y_c \hat{\mathbf{e}}_x - x_c \hat{\mathbf{e}}_y), \quad (10b)$$

where r_g is the waveguide radius and we have assumed $(x_c^2 + y_c^2)^{1/2} \ll r_g$. The motion of the beam's centroid under the influence of the fields in Eqs. (1), (9) and (10) is in the linear approximation governed by

$$\begin{aligned} \frac{d^2 x_c}{dt^2} + \Omega_o \frac{dy_c}{dt} - v_o k_q \Omega_q (x_c \cos k_q z + y_c \sin k_q z) - v_o^2 k_s^2 x_c \\ = \frac{|e|}{\gamma_o m_o c} \left(\frac{\partial}{\partial t} + v_o \frac{\partial}{\partial z} \right) A_x, \end{aligned} \quad (11a)$$

$$\begin{aligned} \frac{d^2 y_c}{dt^2} - \Omega_o \frac{dx_c}{dt} + v_o k_q \Omega_q (y_c \cos k_q z - x_c \sin k_q z) - v_o^2 k_s^2 y_c \\ = \frac{|e|}{\gamma_o m_o c} \left(\frac{\partial}{\partial t} + v_o \frac{\partial}{\partial z} \right) A_y, \end{aligned} \quad (11b)$$

where $\Omega_o = |e|B_o/\gamma_o m_o c$ is the relativistic cyclotron frequency associated with the axial field, $\Omega_q = |e|B_q/\gamma_o m_o c$ is the relativistic cyclotron frequency associated with the rotating quadrupole field, $\gamma_o = (1 - \beta_o^2)^{-1/2}$ is the relativistic mass factor, $k_s = (2\nu/(\beta_o^2 \gamma_o^3 r_g^2))^{1/2}$, $z = z_o + v_o t$, and A_x , A_y are the x and y components of the vector potential given in (1). For the purpose here, we will approximate the exact expressions of (1) by the fields on axis,

$$\frac{|e|}{m_o c^2} \mathbf{A}_{\pm}(x=0, y=0, z) = a_{\pm} e^{ik_{\pm} z} \hat{\mathbf{e}}_{\pm},$$

where k_{\pm} are the axial wave numbers.

The orbit equations for the beam's centroid can be written in a more convenient form. Setting $\xi = x_c + iy_c$, Eqs. (11a,b) become

$$\left(\frac{\partial^2}{\partial z^2} - iK_o \frac{\partial}{\partial z} - k_s^2 \right) \xi - K_q k_q e^{ik_q z} \xi^* = F \quad (12)$$

where $K_o = \Omega_o/v_o$, $K_q = \Omega_q/v_o$, and

$$\begin{aligned} F = \frac{1}{\beta_o \gamma_o} \left[-i(k_+^* - \omega/v_o) a_+^* e^{-i(k_+^* - \omega/v_o)z} e^{-i\omega z_o/v_o} \right. \\ \left. + i(k_- - \omega/v_o) a_- e^{i(k_- - \omega/v_o)z} e^{i\omega z_o/v_o} \right]. \end{aligned} \quad (13)$$

It is convenient at this point to introduce a transformation from the quantity ξ to $\hat{\xi}$

$$\xi = \hat{\xi} e^{+ik_q z/2}. \quad (14)$$

Substituting (14) into (13) transforms the beam's centroid equation into

$$\left[\frac{\partial^2}{\partial z^2} - iK_1 \frac{\partial}{\partial z} + K_2^2 \right] \hat{\xi} - K_3^2 \hat{\xi}^* = G, \quad (15)$$

where $K_1 = K_0 - k_q$, $K_2^2 = (K_0 - k_q/2)k_q/2 - k_q^2$, $K_3^2 = K_q k_q$ and $G = F \exp(-ik_q z/2)$.

Equation(15) can be written in the form

$$\left[\frac{\partial^4}{\partial z^4} + (2K_2^2 + K_1^2) \frac{\partial^2}{\partial z^2} + (K_2^4 - K_3^4) \right] \hat{\xi} = H, \quad (16a)$$

where

$$\begin{aligned} H &= \left[\frac{\partial^4}{\partial z^4} + iK_1 \frac{\partial^2}{\partial z^2} + K_2^2 \right] G + K_3^2 G^* \\ &= e^{-ik_q z/2} \left[\frac{\partial^2}{\partial z^2} + i(K_1 - k_q) \frac{\partial}{\partial z} + ((K_1 - k_q/2)k_q/2 + K_2^2) \right] F \\ &\quad + K_3^2 F^* e^{ik_q z/2}. \end{aligned} \quad (16b)$$

Substituting (13) into (16b) yields

$$\begin{aligned} H &= \frac{i}{\beta_0 \gamma_0} \left[(K_+^* - k_q/2) D_+^* a_+^* e^{-iK_+^* z} - (K_-^* + k_q/2) K_3^2 a_-^* e^{-iK_-^* z} \right] e^{-i\omega z_n/v_0} \\ &\quad - \frac{i}{\beta_0 \gamma_0} \left[(K_- - k_q/2) D_- a_- e^{iK_- z} - (K_+ + k_q/2) K_3^2 a_+ e^{iK_+ z} \right] e^{i\omega z_n/v_0}, \end{aligned} \quad (17)$$

where $K_{\pm} = k_{\pm} - \omega/v_0 \pm k_q/2$ and $D_{\pm} = K_{\pm}^2 \mp K_1 K_{\pm} - K_2^2$. The particular solution to (16a) is

$$\begin{aligned} \hat{\xi} &= \left(\alpha_+^* a_+^* e^{-iK_+^* z} + \beta_-^* a_-^* e^{-iK_-^* z} \right) e^{-i\omega z_n/v_0} \\ &\quad + \left(\alpha_- a_- e^{iK_- z} + \beta_+ a_+ e^{iK_+ z} \right) e^{i\omega z_n/v_0}, \end{aligned} \quad (18a)$$

where

$$\begin{aligned} \alpha_{\pm} &= -\frac{i}{\beta_0 \gamma_0} D_{\pm} (k_{\pm} - \omega/v_0) / R_{\pm}, \\ \beta_{\pm} &= -K_3^2 \alpha_{\pm} / D_{\pm}, \\ R_{\pm} &= K_{\pm}^4 - (2K_2^2 + K_1^2) K_{\pm}^2 + K_2^4 - K_3^4 \\ &= (K_{\pm}^2 - (d_1^2 + d_2^2)) (K_{\pm}^2 - (d_1^2 - d_2^2)), \\ d_1^2 &= K_2^2 + K_1^2/2, \\ d_2^2 &= ((K_2^2 + K_1^2/2)^2 - (K_2^4 - K_3^4))^{1/2}. \end{aligned} \quad (18b-f)$$

Substituting Eqs. (18) together with (14) into Eq. (8), the right-hand side of the wave equation becomes

$$-\frac{4\pi}{c} \int_0^{2\pi/\omega} \frac{dt}{2\pi/\omega} (J_{cx} \mp iJ_{cy}) e^{i\omega t} = 4\pi i \nu \beta_0 \frac{m_0 c^2}{|e|} \delta(x) \delta(y) e^{i\omega z/v_0} \left[(K_{\pm} \mp k_q/2) \alpha_{\pm} a_{\pm} e^{i(K_{\pm} \mp k_q/2)z} + (K_{\mp} \mp k_q/2) \beta_{\mp} a_{\mp} e^{i(K_{\mp} \mp k_q/2)z} \right]. \quad (19)$$

Dispersion Relation

To obtain the dispersion relation the coupled differential equation must be solved, subject to the boundary conditions on the waveguide. To this end, we assume that the electron beam propagates within a perfectly conducting cylindrical waveguide of radius r_g . In general, the complex amplitude for the right- and left-hand circularly polarized TE waves are written as,

$$\mathbf{A}_{\pm}(r, \theta, z) e^{-i\omega t} = \sum_{n,m} b_{\pm nm} [J_{n-1}(\mu_{nm} r) \hat{\mathbf{e}}_{\pm} + J_{n+1}(\mu_{nm} r) e^{\pm i2\theta} \hat{\mathbf{e}}_{\mp}] \exp[i(k_{\pm nm} z \pm (n-1)\theta - \omega t)], \quad (20)$$

where J_n is the n th order Bessel function, $b_{\pm nm}$ are complex constants, μ_{nm} are real constants determined by the boundary conditions and $n = 1, 2, 3, \dots$ and $m = 1, 2, 3, \dots$ are waveguide mode indices.

The boundary condition is such that the tangential component of the electric field vanishes on the waveguide surface, $r = r_g$. At $r = r_g$ we have $\mathbf{E} \cdot \hat{\mathbf{e}}_{\theta} = 0$, where \mathbf{E} is the total electric field and $\hat{\mathbf{e}}_{\theta} = -i \exp(-i\theta) \hat{\mathbf{e}}_{+} + i \exp(-i\theta) \hat{\mathbf{e}}_{-}$ is the unit vector in the azimuthal direction. Applying the boundary condition at $r = r_g$, we find the condition $J'_n(\mu_{nm} r_g) = 0$, so that $\mu_{nm} r_g$ equals the m th positive zero of J'_n .

Since \mathbf{A} is driven by an effective transverse line current, we expect TE_{1m} modes will be excited. Substituting the TE_{1m} mode representation into the left-hand side of Eq. (4), we obtain two sets of coupled equations.

$$\begin{aligned}
& \sum_m e^{ik_{\pm 1m}z} \left(\frac{\omega^2}{c^2} - k_{\pm 1m}^2 - \mu_{1m}^2 \right) J_0(\mu_{1m}r) b_{\pm 1m} \\
& \sum_m e^{ik_{\mp 1m}z} \left(\frac{\omega^2}{c^2} - k_{\mp 1m}^2 - \mu_{1m}^2 \right) J_2(\mu_{1m}r) e^{\mp i2\theta} b_{\mp 1m} \\
& = -\frac{4\pi}{c} \frac{|e|}{m_0 c^2} \int_0^{2\pi/\omega} \frac{dt}{2\pi/\omega} e^{i\omega t} (J_x \mp iJ_y) \Big|_{r=0}. \quad (21)
\end{aligned}$$

Operating on Eq. (21) by both $\int_0^{2\pi} d\theta \int_0^{r_g} J_0(\mu_{1m}r) r dr$ and $\int_0^{2\pi} d\theta e^{\mp i2\theta} \int_0^{r_g} J_2(\mu_{1m}r) r dr$ and solving for $b_{\pm 1m}$, we find that

$$\begin{aligned}
\left(\frac{\omega^2}{c^2} - k_{\pm 1m}^2 - \mu_{1m}^2 \right) b_{\pm 1m} e^{ik_{\pm 1m}z} &= -\frac{2}{c} \frac{1}{I_{1m}} \frac{|e|}{m_0 c^2} \int_0^{2\pi} d\theta \int_0^{r_g} r dr \int_0^{2\pi/\omega} \frac{dt}{2\pi/\omega} e^{i\omega t} \\
& \quad [J_0(\mu_{1m}r) (J_x \mp iJ_y)|_{r=0} + J_2(\mu_{1m}r) (J_x \pm iJ_y)|_{r=0} e^{\mp i2\theta}]. \quad (22)
\end{aligned}$$

where $I_{1m} = \int_0^{r_g} [J_0^2(\mu_{1m}r) + J_2^2(\mu_{1m}r)] r dr = (\mu_{1m}^2 r_g^2 - 1) \mu_{1m}^{-2} J_1^2(\mu_{1m} r_g)$.

The dispersion relation greatly simplifies when only one waveguide mode, say the TE_{11} , takes part in the interaction, i.e., $n = 1$, $m = 1$, $a_{\pm} = b_{\pm 11}$, $k_{\pm} = k_{\pm 11}$.

Substituting (19) into the right-hand-side of (22), we obtain

$$\begin{aligned}
& \left[\left(\frac{\omega^2}{c^2} - k_{\pm 11}^2 - \mu_{11}^2 \right) R_{\pm} - k_b^2 \left(k_{\pm} - \frac{\omega}{v_0} \right)^2 D_{\pm} \right] b_{\pm 11} e^{ik_{\pm}z} \\
& = -k_b^2 K_3^2 \left(k_{\pm} - \frac{\omega}{v_0} \right) \left(k_{\mp} - \frac{\omega}{v_0} \mp k_q \right) b_{\mp 11} e^{i(k_{\mp} \mp k_q)z}, \quad (23)
\end{aligned}$$

where $k_b^2 = 2\nu/\gamma_0 I_{11} = 2\nu\mu_{11}^2/(\gamma_0(\mu_{11}^2 r_g^2 - 1)J_1^2(\mu_{11} r_g))$. The RH and LH circularly polarized waves are simultaneously excited only when $k_{+} = k_{-} - k_q$. Eliminating $b_{\pm 11}$, the dispersion relation coupling the RH and LH circularly polarized waves becomes

$$\begin{aligned}
& \left[R - \frac{k_b^2 (k - \omega/v_0 + k_q)^2 D_{-}}{\omega^2/c^2 - (k + k_q)^2 - \mu_{11}^2} \right] \left[R - \frac{k_b^2 (k - \omega/v_0)^2 D_{+}}{\omega^2/c^2 - k^2 - \mu_{11}^2} \right] \\
& = k_b^4 K_3^4 \left(\frac{(k - \omega/v_0)^2}{\omega^2/c^2 - k^2 - \mu_{11}^2} \right) \left(\frac{(k - \omega/v_0 + k_q)^2}{\omega^2/c^2 - (k + k_q)^2 - \mu_{11}^2} \right). \quad (24)
\end{aligned}$$

where $k = k_+$, $k_- = k + k_q$, $K = K_{\pm} = k - \omega/v_o + k_q/2$, $D_{\pm} = K^2 \mp K_1 K - K_2^2$ and $R = R_{\pm} = D_+ D_- - K_3^4 = K^4 - (2K_2^2 + K_1^2)K^2 + K_2^4 - K_3^4$. Equation (24) can be put into the form

$$\left[D_+ - \frac{k_b^2(k - \omega/v_o + k_q)^2}{\omega^2/c^2 - (k + k_q)^2 - \mu_{11}^2} \right] \left[D_- - \frac{k_b^2(k - \omega/v_o)^2}{\omega^2/c^2 - k^2 - \mu_{11}^2} \right] - K_3^4 = 0, \quad (25a)$$

and/or

$$R = 0. \quad (25b)$$

Equation (25a) agrees with the dispersion relation in Ref. 9 with the vertical field set to zero. Equation (25b) is the dispersion relation of the hybrid cyclotron and quadrupole modes with image fields in a waveguide in the absence of electromagnetic fields.

The dispersion relation possesses the following symmetry:

$$(k, k_q, B_o) \Longleftrightarrow (k - k_q, -k_q, -B_o).$$

Utilizing this symmetry condition, the discussions in Section III can also be applied to rotating quadrupoles of the opposite helicity. The polarization of the waveguide mode associated with the wave number k that the three-wave is unstable is determined by the polarization of the waveguide mode that intersects the unstable beam modes.

The modes taking part in the interaction can be conveniently classified by setting the beam current equal to zero. The dispersion relation, for zero beam current, reduces to

$$\begin{aligned} & [k^2 - \omega^2/c^2 + \mu_{11}^2] [(k + k_q)^2 - \omega^2/c^2 + \mu_{11}^2] \\ & [(k - \omega/v_o + k_q/2)^2 - (d_1^2 + d_2^2)] [(k - \omega/v_o + k_q/2)^2 - (d_1^2 - d_2^2)] = 0, \end{aligned} \quad (26)$$

where

$$\begin{aligned} d_1^2 &= \frac{1}{2}(K_o(K_o - k_q) + k_q^2/2), \\ d_2^2 &= \frac{1}{2}(K_o^2(K_o - k_q)^2 + 4K_q^2 k_q^2)^{1/2}. \end{aligned}$$

The first and second bracketed terms on the left-hand side of Eq. (26) represents the LH and RH circularly polarized transverse electric waveguide modes, while the third and fourth terms, R , are hybrid cyclotron and quadrupole modes.

A diagram of the dispersion relation in the zero beam current limit is shown in Fig. 2. The parameters for the plot are guide magnetic field $B_o = -1 \text{ kG}$, $k_q = 0.5 \text{ cm}^{-1}$, quadrupole gradient $B_q k_q = 200 \text{ G/cm}$, $\gamma_o = 5$ and drift-tube radius $r_g = 3 \text{ cm}$. The curves are associated with the RH and LH polarized waveguide modes respectively. The cut-off frequency of the waveguide TE_{11} mode is $\mu_{11}c$. The two straight solid (—) lines correspond to the beam lines associated with the $d_1^2 - d_2^2$ expressions, and the two dashed (- -) lines correspond to the beam lines associated with the $d_1^2 + d_2^2$ expression.

III. STABILITY REGIMES AND ANALYTICAL EXPRESSIONS FOR GROWTH RATES

The dispersion relation, Eq. (25a), contains i) a region of orbital instability (in the absence of the electromagnetic waves), ii) regions of three-wave instability, and iii) regions of stability. In this section, we will obtain the conditions delineating the various regimes and find analytical expressions for the maximum growth rate in each of the three-wave unstable regions. The stability diagrams are obtained in (k_q, K_o) space for given values of γ_o , r_g and $B_q k_q$ in the limit of zero beam current.

Orbit Unstable Regime

The expression $R = 0$ is the dispersion relation for the particle dynamics in the presence of stellarator windings with an axial magnetic field. This expression is in agreement with Eq. (10) of Ref. 2 in the limit of perfectly conducting walls. The electron beam in this configuration can be unstable when $(d_1^2 - d_2^2) \leq 0$. The unstable values of K_o are

$$K_{crit,2} = \frac{k_q}{2} - 2K_q \leq K_o \leq K_{crit,3} = \frac{k_q}{2} + 2K_q, \quad (27)$$

where $K_q = \Omega_q/v_o$, $\Omega_q = |e|B_q/\gamma_o m_o c$, $K_o = \Omega_o/v_o$ and $\Omega_o = |e|B_o/\gamma_o m_o c$. Equation (27) is in agreement with the stability condition of Ref. 1 in the limit of straight cylindrical geometry and zero beam current. It is interesting to note that this condition is also in agreement with the condition for beam envelope stability in the limit of zero space charge.¹³

Three-Wave Unstable Regimes

The three-wave instability will occur when, for example, the RHCP waveguide mode intersects, in the (ω, k) plane, the appropriate beam mode given by

$$(k - \omega/v_o + k_q/2)^2 - (d_1^2 - d_2^2) = 0, \quad (28)$$

and $(d_1^2 - d_2^2) > 0$. For $k_q > 0$, the instability for the RHCP waveguide mode occurs for $\omega > 0$. For $K_o < K_{crit,2}$, the three-wave is unstable (Region I) when the RHCP waveguide mode intersects the beam line $\omega/v_o = (k + k_q/2) + \sqrt{d_1^2 - d_2^2}$. For $K_o > K_{crit,3}$, the three-wave is unstable (Region II) when the RHCP waveguide mode intersects the beam line

$\omega/v_o = (k + k_q/2) - \sqrt{d_1^2 - d_2^2}$. Identical three-wave instability growth rates occur for the LHCP waveguide mode, for ω/c with sign opposite to the unstable modes associated with the RHCP waveguide mode.

Three-Wave Stable Regime for $K_o < K_{crit,2}$

Stability is achieved when the waveguide cut off frequency $\mu_{11}c$ is sufficiently large so that intersection with either of the beam lines, defined by Eq. (28) cannot be achieved. The condition in terms of the waveguide mode cutoff is

$$q\mu_{11} \geq k_q + 2(d_1^2 - d_2^2)^{1/2}, \quad (29)$$

where

$$q = \left(\frac{4}{\gamma_o^2 - 2} \right)^{1/2}.$$

Based on Eq. (29), the region of

$$k_q > q\mu_{11} \quad \text{and} \quad K_o < K_{crit,2} \quad (30)$$

is always three-wave unstable. If the inequality in (29) can be satisfied, we can solve for the explicit value of K_o for the three-wave stable regime.

For $k_q < q\mu_{11}$ and $K_o < K_{crit,2}$, condition for stability in terms of the variable K_o is

$$2fK_o(K_o - k_q) + f^2 - 4K_qk_q < 0, \quad (31)$$

where

$$f = q\mu_{11}(k_q - q\mu_{11}/2). \quad (32)$$

Defining

$$\zeta = k_q^2(1 + 8K_q^2f) - 2f, \quad (33)$$

we solve for K_o with $k_q < q\mu_{11}$, and find four situations:

i) for $f > 0$ and $\zeta > 0$, the stable range of K_o is given by

$$K_{crit,1} = \frac{k_q}{2} - \frac{\zeta^{1/2}}{2} < K_o < K_{crit,2}, \quad (34a)$$

ii) for $f < 0$ and $\zeta > 0$, the stable values of K_o are

$$K_o < K_{crit,1} = \text{smaller of } \left(\frac{k_q}{2} - \frac{\zeta^{1/2}}{2}, K_{crit,2} \right), \quad (34b)$$

iii) for $f > 0$ and $\zeta < 0$, all values of

$$K_o < K_{crit,2} \quad (34c)$$

are unstable,

iv) for $f < 0$ and $\zeta < 0$, all values of

$$K_o < K_{crit,2} \quad (34d)$$

are stable.

Three-Wave Stable Regime for $K_o > K_{crit,3}$

The three-wave interaction is also stable when the RHCP waveguide mode intersects only the top (the beam line with larger ω for the same k) but not the bottom beam mode associated with Eq. (28), and $K_o > K_{crit,3}$. This occurs when

$$q\mu_{11} \geq k_q - 2(d_1^2 - d_2^2)^{1/2}. \quad (35)$$

The three-wave interaction is stable for

$$k_q < q\mu_{11} \quad \text{and} \quad K_o > K_{crit,3}. \quad (36)$$

For $k_q > q\mu_{11}$ and $K_o > K_{crit,3}$, the values of K_o that are three-wave stable are

$$K_o > K_{crit,4} = \frac{k_q}{2} + \frac{\zeta^{1/2}}{2}. \quad (37)$$

In this regime, one can show that $f > 0$ and $\zeta > 0$. In the limit of small quadrupole gradient, large γ_o and $K_o > K_{crit,3}$, the stability condition is approximately¹¹

$$K_o > k_q - \mu_{11}/\gamma_o. \quad (38)$$

The various operating regimes are illustrated as functions of k_q and K_o in Fig. 3, for $\gamma_o = 5$, $r_g = 3$ cm and quadrupole gradient $B_q k_q = 200$ G/cm. This plot assumes that the quadrupole gradient is a constant, and (k_q, K_o) are allowed to vary. The horizontal separation of the boundaries for the orbital unstable region is $4K_q$. Since the stability boundaries are obtained in the limit of zero beam current, the area of the actual stable regions will shrink slightly as the value of the current is increased.

Analytical Expressions for the Growth Rates

In the three-wave unstable regimes, we can obtain analytical expressions for the peak growth rates. The dispersion relation (25a) for the coupled RH and LH polarized wave can be rewritten as

$$(\omega^2 - \omega_1^2)((\omega - \omega_2)^2 - \Delta\omega_1^2)((\omega - \omega_2)^2 - \Delta\omega_2^2)(\omega^2 - \omega_3^2) = \bar{\sigma}, \quad (39)$$

where

$$\bar{\sigma} = k_b^2 v_o^2 c^2 [(\omega - v_o k)^2 (\omega^2 - \omega_3^2) D_+ + (\omega - v_o(k + k_q))^2 (\omega^2 - \omega_1^2) D_-],$$

$\omega_1 = \sqrt{k^2 + \mu_{11}^2} c$, $\omega_2 = v_o(k + k_q/2)$, $\omega_3 = \sqrt{(k + k_q)^2 + \mu_{11}^2} c$, $\Delta\omega_1^2 = v_o^2(d_1^2 + d_2^2)$, and $\Delta\omega_2^2 = v_o^2(d_1^2 - d_2^2)$. Based on the numerical results of the full dispersion relation in Eq. (25a), instability occurs at the intersection of the RHCP waveguide mode and one of the two modes of Eq. (28) for $k_q > 0$ and $\omega > 0$. Defining $\omega = \omega_1 + \delta\omega$ and $\sigma = \bar{\sigma}|_{\omega=\omega_1}$, the dispersion relation reduces to

$$(\omega^2 - \omega_1^2)((\omega - \omega_2)^2 - \Delta\omega_1^2)((\omega - \omega_2)^2 - \Delta\omega_2^2) = \sigma, \quad (40)$$

where $\sigma = k_b^2 v_o^2 c^2 (\omega_1 - v_o k)^2 D_+|_{\omega=\omega_1 \pm \Delta\omega_2}$, $D_+|_{\omega=\omega_1 \pm \Delta\omega_2} = (\Delta\omega_2/c)^2 \pm K_1(\Delta\omega_2/c) - K_2^2$ and the top and bottom signs in D_+ refer to the three-wave unstable regions I and II respectively. Equation (40) is the dispersion relation when the RHCP waveguide mode is uncoupled to the LHCP waveguide mode.

The instability region I in Fig. 3 is the result of the waveguide mode intersecting the upper mode (the beam line with larger ω for the same k) given in Eq. (28). We will write

$\omega = \omega_1 + \delta\omega$ and $\omega_1 = \omega_2 + \Delta\omega_2$. We will assume $\Delta\omega_1 - \Delta\omega_2 \gg \delta\omega$. The dispersion relation is given approximately by

$$\left(\frac{\delta\omega}{c} + 2\frac{\Delta\omega_2}{c}\right)\left(\frac{\delta\omega}{c}\right)^2 = -\frac{\sigma/c^3}{2\omega_1} \frac{1}{(\Delta\omega_1^2 - \Delta\omega_2^2)}. \quad (41)$$

For simplicity, we will assume the temporal growth rate is much smaller than the separation of the beam modes, i.e., $\delta\omega \ll 2\Delta\omega_2$. With this assumption, we obtain a simple expression for the dispersion relation,

$$\left(\frac{\delta\omega}{c}\right)^2 \simeq -\frac{\sigma/c^2}{4\omega_1\Delta\omega_2} \frac{1}{(\Delta\omega_1^2 - \Delta\omega_2^2)}. \quad (42)$$

For values of K_o in the unstable region I, i.e., $K_o < K_{crit,2}$, the values of σ are positive, and Eq. (42) gives the temporal growth rate.

When the RHCP waveguide mode intersects both modes given by Eq. (28) with $k_q > 0$, $\omega > 0$ and $K_o > K_{crit,3}$, the instability occurs only at the intersection of the RHCP wave mode and the lower beam mode. This gives the instability regime II in Fig. 3. We will define $\omega_1 = \omega_2 - \Delta\omega_2$. The dispersion relation becomes

$$\left(\frac{\delta\omega}{c} - 2\frac{\Delta\omega_2}{c}\right)\left(\frac{\delta\omega}{c}\right)^2 = -\frac{\sigma/c^3}{2\omega_1} \frac{1}{(\Delta\omega_1^2 - \Delta\omega_2^2)}. \quad (43)$$

Here again, we assume $2\Delta\omega_2 \gg \delta\omega$ and the dispersion relation reduces to

$$\left(\frac{\delta\omega}{c}\right)^2 \simeq \frac{\sigma/c^2}{4\omega_1\Delta\omega_2} \frac{1}{(\Delta\omega_1^2 - \Delta\omega_2^2)}. \quad (44)$$

For $K_{crit,3} < K_o < k_q$, the quantity σ is negative, and Eq. (44) gives the temporal growth rate in region II of Fig. 3. The analytical expressions (42) and (44) show that the temporal growth rate $\Gamma = Im(\delta\omega)$ scales approximately as the square root of the beam current, i.e., $\Gamma/c \propto I_p^{1/2}$.

IV. NUMERICAL RESULTS

The full dispersion relation, Eq. (25a) is solved numerically to: i) obtain the growth rates and group velocities, ii) verify the various operating regimes and the analytical expressions for the temporal growth rates and iii) show the scaling of the growth rate with respect to the various parameters. The numerical studies center around the parameters shown in Table I. With the quadrupole wave number k_q chosen to be 0.5 cm^{-1} ($\lambda_q = 12.57 \text{ cm}$), we may demonstrate each of the different operating regimes by varying the axial magnetic field, B_o , except in one of the stable regimes, where we take $k_q = 0.1 \text{ cm}^{-1}$.

Figure 3 is a plot of the various operating regimes in the parameter space of k_q as a function of K_o for $\gamma_o = 5$, $B_q k_q = 200 \text{ G/cm}$ and $r_g = 3 \text{ cm}$ as in Table I.

Numerical Results from Full Dispersion Relation

The dispersion diagram with current $I_b = 1 \text{ kA}$ for the five different regimes are shown in Fig. 4:

- a) $B_o = -1.0 \text{ kG}$ ($K_o = -0.24 \text{ cm}^{-1}$) and $k_q = 0.5 \text{ cm}^{-1}$ in the three-wave unstable region I,
- b) $B_o = 2.15 \text{ kG}$ ($K_o = 0.26 \text{ cm}^{-1}$) and $k_q = 0.5 \text{ cm}^{-1}$ in the orbit unstable regime,
- c) $B_o = 3.5 \text{ kG}$ ($K_o = 0.42 \text{ cm}^{-1}$) and $k_q = 0.5 \text{ cm}^{-1}$ in the three-wave unstable region II,
- d) $B_o = 5.0 \text{ kG}$ ($K_o = 0.60 \text{ cm}^{-1}$) and $k_q = 0.5 \text{ cm}^{-1}$ in the three-wave stable regime,
- e) $B_o = -5.0 \text{ kG}$ ($K_o = -0.60 \text{ cm}^{-1}$) and $k_q = 0.1 \text{ cm}^{-1}$ in the three-wave stable regime.

Plots of the temporal growth rate as a function of wave number k are given in Figs. 5-7 for each of the different regimes with current $I_b = 1 \text{ kA}$. Figure 5 plots the temporal growth rates in region I, for $B_o = -1.0 \text{ kG}$ ($K_o = -0.12 \text{ cm}^{-1}$), $B_o = 0$, $B_o = 1.0 \text{ kG}$ ($K_o = 0.12 \text{ cm}^{-1}$), and $B_o = 1.3 \text{ kG}$ ($K_o = 0.156 \text{ cm}^{-1}$). Only the growth rates associated with $\text{Re}(\omega) > 0$ are plotted; these are associated with RHCP waves. The growth rates associated with $\text{Re}(\omega) < 0$ are identical and are associated with LHCP waves. The growth rate and the range of unstable values of k increase as K_o approaches the orbit unstable value of $K_{\text{crit},2} = 0.154 \text{ cm}^{-1}$.

Figure 6 shows temporal growth rates in the three-wave unstable region II, for $B_o = 2.95 \text{ kG}$ ($K_o = 0.35 \text{ cm}^{-1}$), $B_o = 3.0 \text{ kG}$ ($K_o = 0.36 \text{ cm}^{-1}$), $B_o = 3.25 \text{ kG}$ ($K_o = 0.39 \text{ cm}^{-1}$) and $B_o = 3.5 \text{ kG}$ ($K_o = 0.41 \text{ cm}^{-1}$). For some values of B_o , the RHCP wave intersects the beam line two times as indicated by temporal growth rates at two separate regions of wave number k for a given axial magnetic field. The growth rate and the range of unstable values of k increases as K_o approaches $K_{crit,3}$. The stability boundaries predict that the three-wave instability is present for $K_{crit,3} = 0.35 \text{ cm}^{-1} < K_o < K_{crit,4} = 0.41 \text{ cm}^{-1}$ ($2.95 \text{ kG} < B_o < 3.5 \text{ kG}$). Numerical results for $I_b = 1 \text{ kA}$ are in excellent agreement with the theory.

Figure 7 plots the temporal growth rate versus k in the orbit unstable region for $B_o = 2.15 \text{ kG}$ ($K_o = 0.26 \text{ cm}^{-1}$). The region of instability covers both positive and negative values of wave number k , even at regions where the beam lines are far from the waveguide mode. Thus, the unstable growth rate is the result of unstable beam orbits in the stellarator and guide fields, irrespective of the electromagnetic waves.

As the beam current increases, the coupling of the RHCP and LHCP waves becomes stronger and the actual stability boundaries deviate from the analytic expressions. Figures 8-10 are plots of temporal growth rate as a function of wave number k for $I_b = 10 \text{ kA}$. Figure 8 plots the temporal growth rates in region I, for $B_o = -1.0 \text{ kG}$ ($K_o = -0.12 \text{ cm}^{-1}$), $B_o = 0$, $B_o = 1.0 \text{ kG}$ ($K_o = 0.12 \text{ cm}^{-1}$), and $B_o = 1.3 \text{ kG}$ ($K_o = 0.156 \text{ cm}^{-1}$).

Figure 9 plots temporal growth rates versus k in the three-wave unstable region II, for $B_o = 3.0 \text{ kG}$ ($K_o = 0.36 \text{ cm}^{-1}$), $B_o = 3.25 \text{ kG}$ ($K_o = 0.39 \text{ cm}^{-1}$), $B_o = 3.5 \text{ kG}$ ($K_o = 0.41 \text{ cm}^{-1}$) and $B_o = 3.85 \text{ kG}$ ($K_o = 0.45 \text{ cm}^{-1}$). The range of B_o for the three-wave unstable region II at zero beam current is $2.95 \text{ kG} < B_o < 3.5 \text{ kG}$. For current of $I_p = 10 \text{ kG}$, the RHCP and LHCP waves become coupled for $B_o = 2.95 - 3.25 \text{ kG}$. At the same time, the three-wave unstable regime is extended beyond $B_o = 3.5 \text{ kG}$ to $B_o = 3.85 \text{ kG}$. The RHCP and LHCP waves become coupled for $B_o = 2.95 - 3.25 \text{ kG}$ and the three-wave unstable regime is extended into a region where $K_o > K_{crit,4} = 0.41 \text{ cm}^{-1}$, where the analytic ($I_b = 0$) expressions predict stability.

Figure 10 plots the temporal growth rate versus k in the orbit unstable region for $B_o = 2.15 \text{ kG}$ ($K_o = 0.26 \text{ cm}^{-1}$). Here the region of instability covers essentially all values

of wave number k .

A summary of peak temporal growth rates as a function of normalized guide field K_o for $I_b = 10 \text{ kA}$ is shown in Fig. 11 for $\gamma_o = 5$, $\gamma_o = 7.5$ and $\gamma_o = 10$. The group of curves on the left belong to unstable region I and the group of curves on the right belong to unstable region II. The gap separating the two groups of curves corresponds to the orbit unstable region. Plots of the group velocity as a function of K_o are shown in Fig. 12. Those values plotted are associated with the growth rates of Fig. 11. The group velocity approaches the beam velocity in three-wave unstable region II.

We also examine the effect of the waveguide radius r_g on the three-wave instability. As the guide radius is increased, the waveguide cut-off frequency $\mu_{11}c$ decreases. For the three-wave unstable region I, the intersection of the waveguide mode and one of the beam lines in Eq. (28) can occur for negative values of wave number k . When this occurs, the phase velocity is negative and group velocity is positive but reduced in value. Figure 13 plots the temporal growth rate and the group velocity as a function of K_o for $r_g = 5 \text{ cm}$ and $I_b = 10 \text{ kA}$, while keeping all the other parameters the same as in Table I.

Comparison of Analytic and Numerical Results

The analytical expressions for the temporal growth rates for the two regions of the three-wave instability are given in Eq. (42) and (44). Figure 14 is a comparison of the maximum temporal growth rate as a function of the normalized guide field K_o for the values obtained from the numerically solved full dispersion relation (solid curves) and from the analytical expressions (dashed curves) for current $I_b = 1 \text{ kA}$. The agreement between the analytical and numerical results of the temporal growth rates is good as long as $\Delta\omega_2/c > \Gamma/c$ (see Eqs. (39)-(44)). On the dispersion diagram, $2\Delta\omega_2/c$ is the difference in frequency/ c of the beam lines (28) that could go unstable. To illustrate the case $\Delta\omega_2/c > \Gamma/c$, we take $K_o = -0.36 \text{ cm}^{-1}$ ($B_o = -3 \text{ kG}$). The numerical result of the temporal growth rate is $\Gamma/c = 4.3 \times 10^{-3} \text{ cm}^{-1}$, which is much smaller than $\Delta\omega_2/c = 0.25$. The analytical result for the temporal growth rate is also $\Gamma/c = 4.3 \times 10^{-3} \text{ cm}^{-1}$. As $\Delta\omega_2/c$ decreases and Γ/c increases, the analytical expressions for the growth rate becomes less accurate. At $K_o = 0.12 \text{ cm}^{-1}$ ($B_o = 1 \text{ kG}$), $\Delta\omega_2/c = 8.2 \times 10^{-2}$, which is comparable to

Γ/c . The analytical expression for the growth rate, $\Gamma/c = 2.50 \times 10^{-2} \text{ cm}^{-1}$, is 8% larger than the numerical result of $\Gamma/c = 2.30 \times 10^{-2} \text{ cm}^{-1}$.

V. CONCLUSIONS

The addition of stellarator windings to an axial guide field was proposed as a method of transporting a high current beam in a curved geometry with a high tolerance to energy mismatch.¹ The stability properties of such configurations have been clarified in the present study, which included the beam centroid motion, the electromagnetic waveguide modes, expressed in terms of right-hand circularly polarized (RHCP) and left-hand circularly polarized (LHCP) waves, and the induced image forces on the conducting boundaries, in addition to the external magnetic fields.

We find five operating regimes: i) two physically distinct three-wave unstable regimes, ii) an orbit unstable regime, in which the beam centroid is unstable independent of the electromagnetic waveguide modes and iii) two stable regimes. We have obtained analytical expressions for the boundaries of the various stability regimes in parameter space and have presented algebraic expressions for the growth rates in each of the two three-wave unstable regimes. These analytical results are valid in the limit of low beam current, when the RHCP and LHCP waves decouple, and are in good agreement with those obtained via numerical solutions of the full dispersion relation.

The simplified dispersion relation for uncoupled RHCP and LHCP waves, given in Eq. (40), has been shown to produce results that are in close agreement with those of the full dispersion relation. The simplified dispersion relation is not valid, however, when the coupling between the RHCP and LHCP waves is strong, as in the orbit unstable regime. In three-wave unstable region II, the coupling is strong only at high current. The growth rates in this regime, for example, from the full (coupled) dispersion relation are about 20 – 30% larger than from the uncoupled dispersion relation for $k_w = 0.5 \text{ cm}^{-1}$ and $I = 10 \text{ kA}$. In three-wave unstable region I the RHCP and LHCP waves are essentially uncoupled.

These results suggest that the three-wave instability can be avoided by appropriately choosing the various parameters. Results show that as the beam energy increases, the stability conditions become more restrictive. In such cases, it may be necessary to decrease the quadrupole gradient, $B_q k_q$, quadrupole wave number k_q and/or increase the value of the guide field B_0 in order to remain in the stable regime.

Acknowledgments

This work is supported by DARPA and ONR. We also like to thank D. Chernin, A. Mondelli and T. Hughes for their insight and T. Swyden for his assistance.

References

1. C. W. Roberson, A. Mondelli and D. Chernin, Phys. Rev. Lett. 50, 507 (1983).
2. P. Sprangle and C. A. Kapetanakis, Part. Accel. 18, 203 (1986).
3. J. Golden, J. Pasour, D. E. Pershing, T. Smith, F. Mako, S. Slinker, F. Moro, N. Orrick, R. Altes, A. Fliflet, P. Champney and C. A. Kapetanakis, IEEE Trans. on Nucl. Sci. NS-30, 2114 (1983).
4. A. Mondelli, D. Chernin, S. D. Putnam, L. Schlitt and V. Bailey, Proc. Sixth Intl. Conf. on High Power Part. Beams (Osaka, Japan), (1986).
5. V. Bailey, L. Schlitt, M. Tiefenback, S. Putnam, A. Mondelli, D. Chernin and J. Petillo, Proc. of the 1987 IEEE Particle Accel. Conf., Ed. E. R. Lindstrom and L. S. Taylor, 920 (1987).
6. S. D. Putnam, Proc. of the 1987 IEEE Particle Accel. Conf., Ed. E. R. Lindstrom and L. S. Taylor, 887 (1987).
7. Private communications with C. Kapetanakis.
8. B. Levush, T. M. Antonsen, W. M. Manheimer and P. Sprangle, NRL Memorandum Report 5471 (1984) and Phys. Fluids 28, 7 (1985).
9. T. P. Hughes and B. B. Godfrey, Phys. Fluids 29, 1698 (1986).
10. P. Sprangle, C. M. Tang and C. W. Roberson, Nuclear Instr. and Methods in Phys. Research A239, 1 (1985).
11. Private communications with D. Chernin and T. Hughes.
12. B. B. Godfrey and T. P. Hughes, "Quadrupole Focusing Instability Growth Rate Expressions", MRC/ABQ-R-1011 (Mission Research Corporation, Albuquerque, NM. Jan. 1988).
13. D. Chernin, Part. Accel. 24, 29 (1988).

Table I: Parameters Used in Section IV

Quadrupole gradient, $B_q k_q$	200 G/cm
Beam energy (γ_o)	5
Beam current, I_b	1,10 kA
Drift-tube radius, r_g	3 cm

Calculated parameters

TE_{11} cut-off frequency/c, μ_{11}	0.614 cm^{-1}
$q\mu_{11}$	0.256 cm^{-1}
$K_q k_q$	0.024 cm^{-2}
$\beta_o = v_o/c$	0.9793

For rotating quadrupole wavelength, $\lambda_q = 12.57 \text{ cm}$

Wave number, k_q	0.5 cm^{-1}
K_q	0.048 cm^{-1}
$K_{\text{crit},2} (B_o = 1.32 \text{ kG})$	0.154 cm^{-1}
$K_{\text{crit},3} (B_o = 2.95 \text{ kG})$	0.346 cm^{-1}
$K_{\text{crit},4} (B_o = 3.52 \text{ kG})$	0.413 cm^{-1}

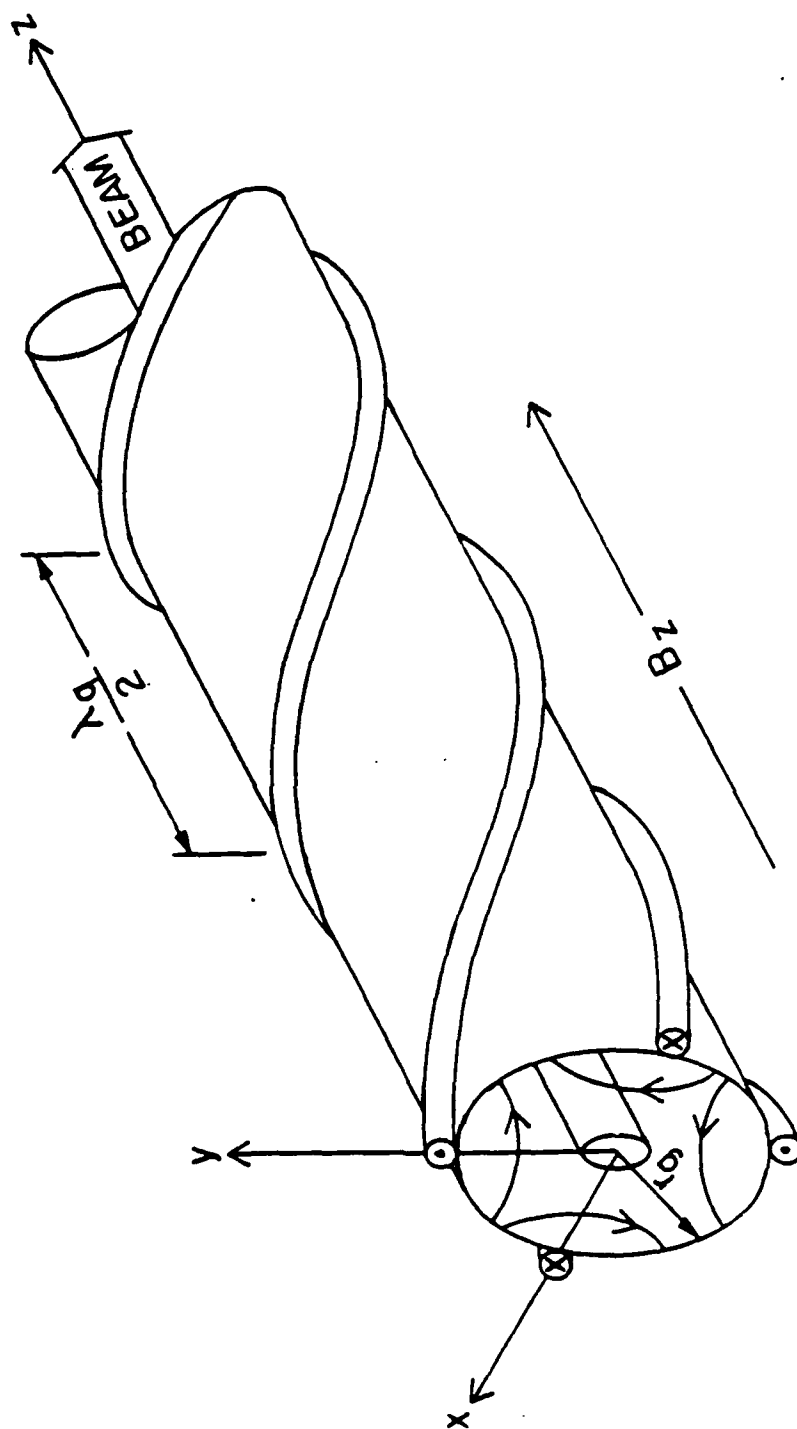


Fig. 1 The geometry showing the conducting cylindrical drift tube, the rotating quadrupole field and the axial guide field.

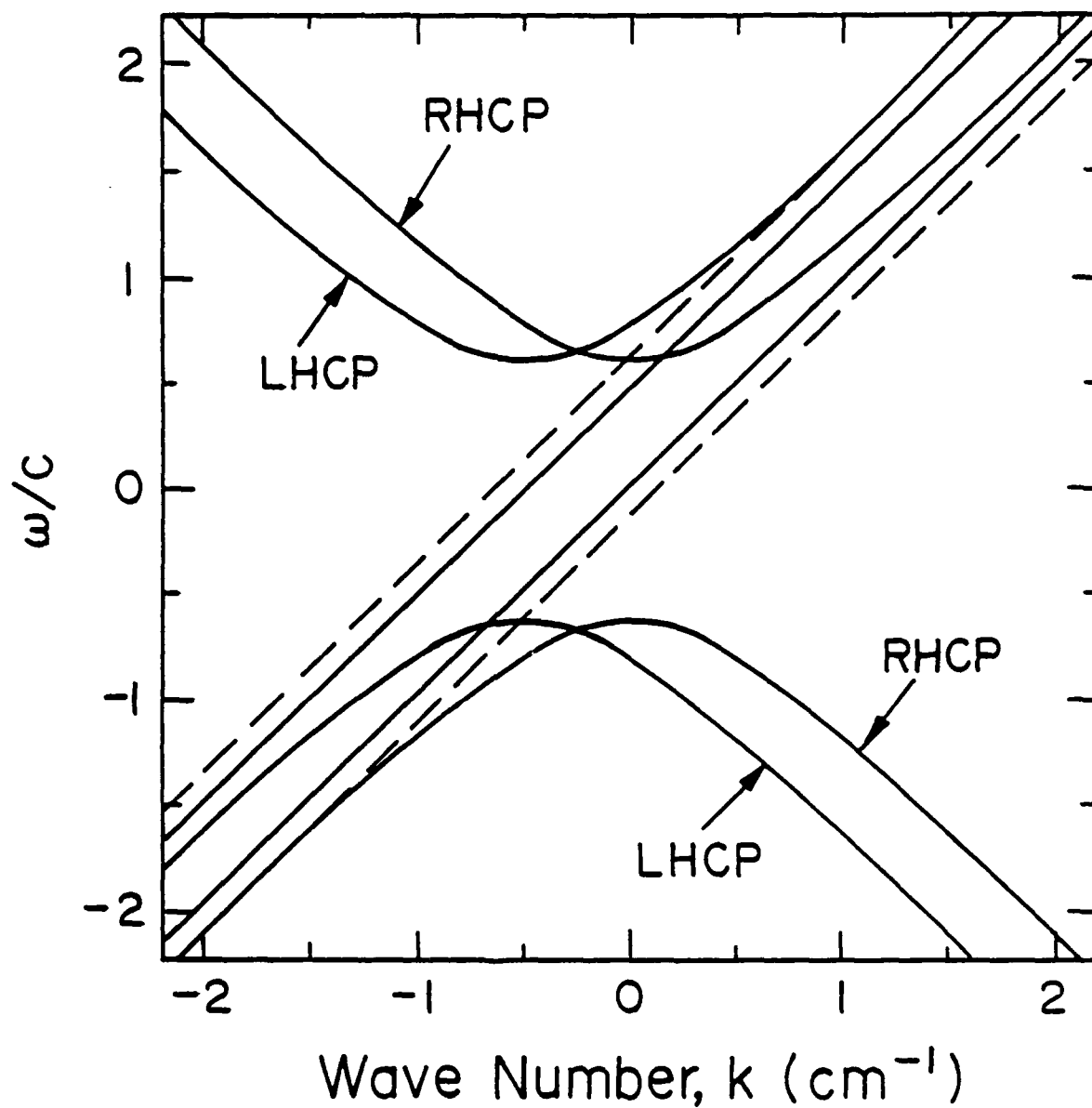


Fig. 2 The dispersion diagram in the limit of zero beam current. The curves are the LH and RH circularly polarized TE_{11} waveguide modes. The dashed (---) and solid (—) straight lines are the beam modes.

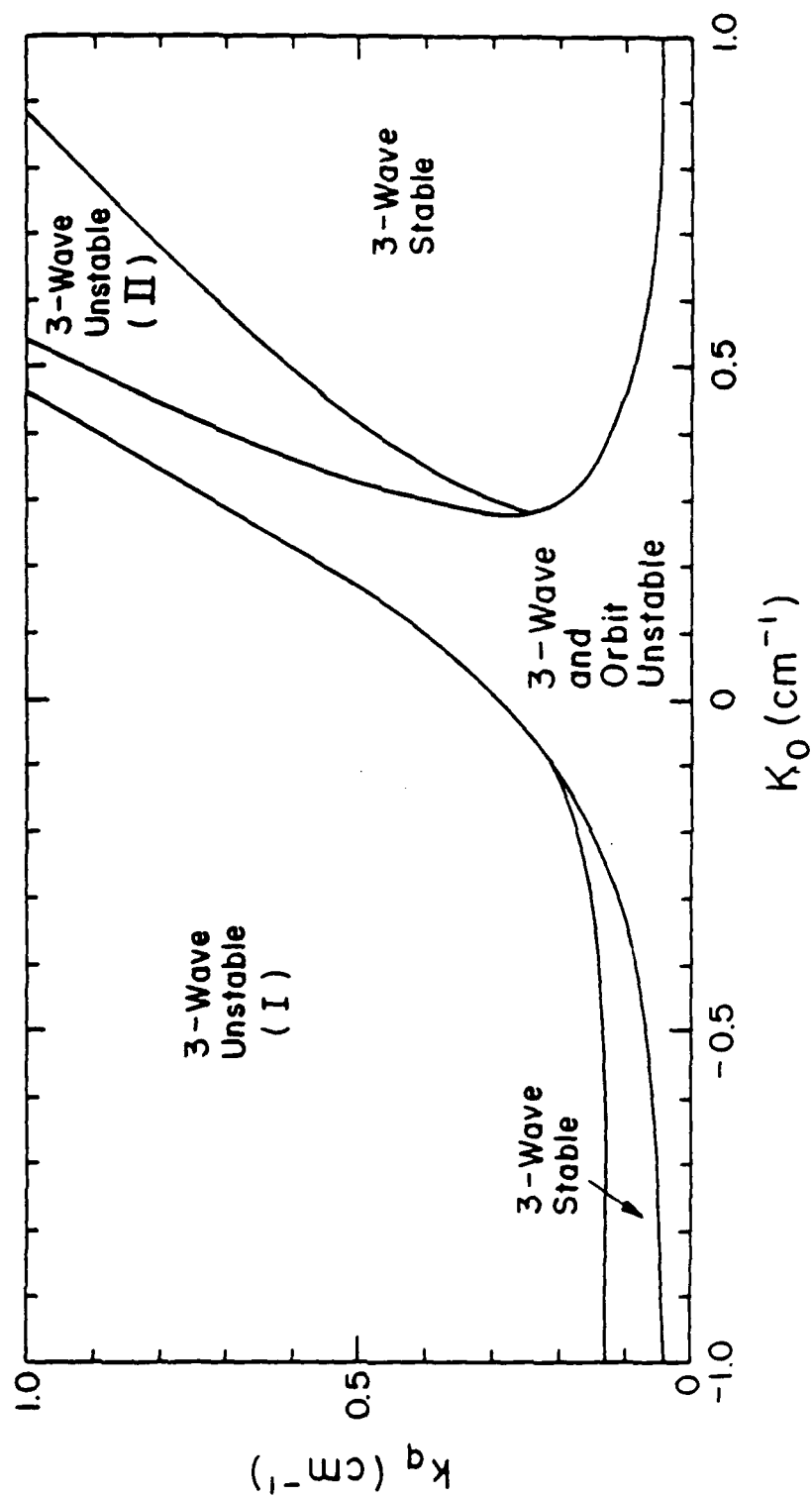


Fig. 3 Plot of (k_q, K_o) parameter space showing the various operating regimes. Stability boundaries are calculated from Eqs. (27)-(37) for parameters of Table I.

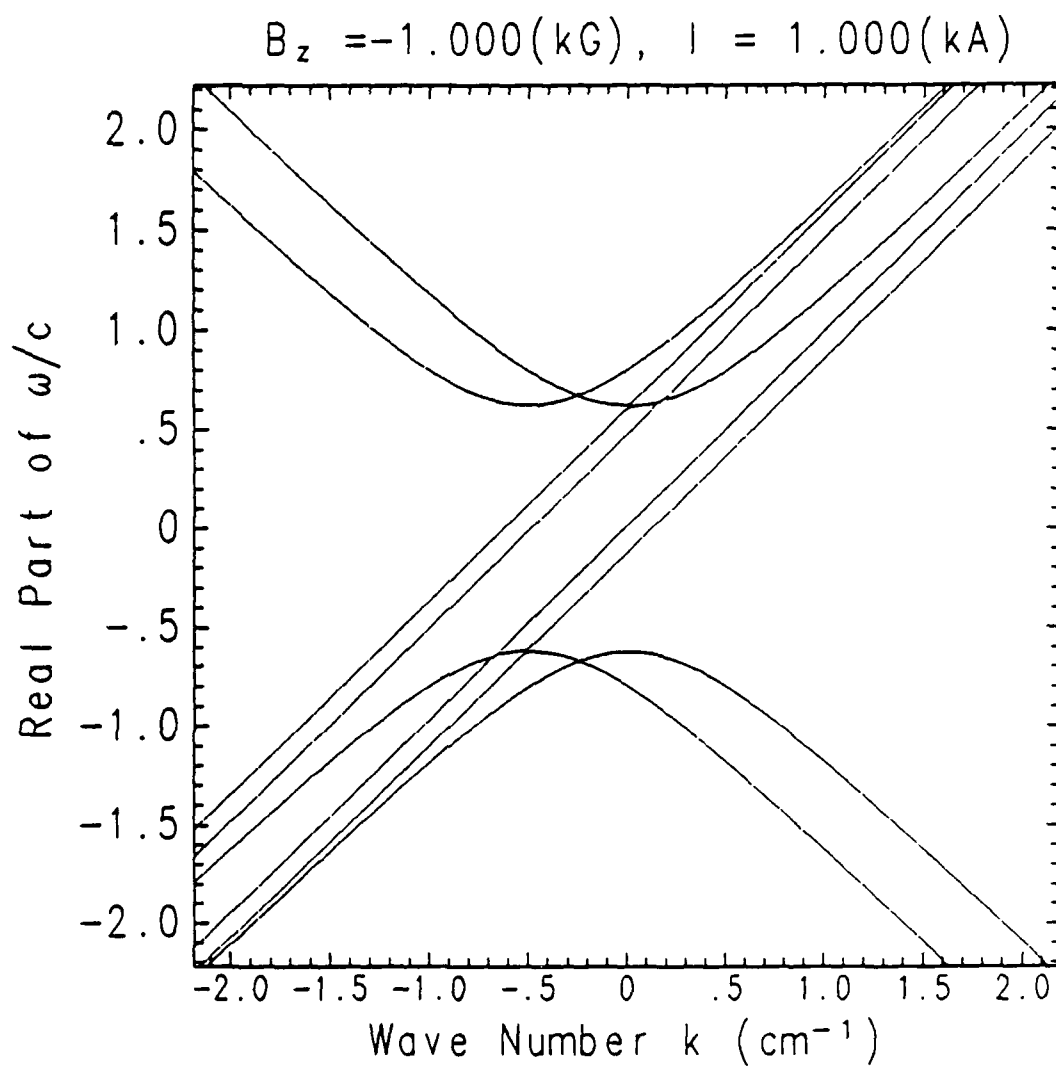


Fig. 4 Dispersion diagram for the right-hand-circularly polarized waves for parameters in Table I with:

a) $B_o = -1.0 \text{ kG}$ ($K_o = -0.24 \text{ cm}^{-1}$) and $k_q = 0.5 \text{ cm}^{-1}$.

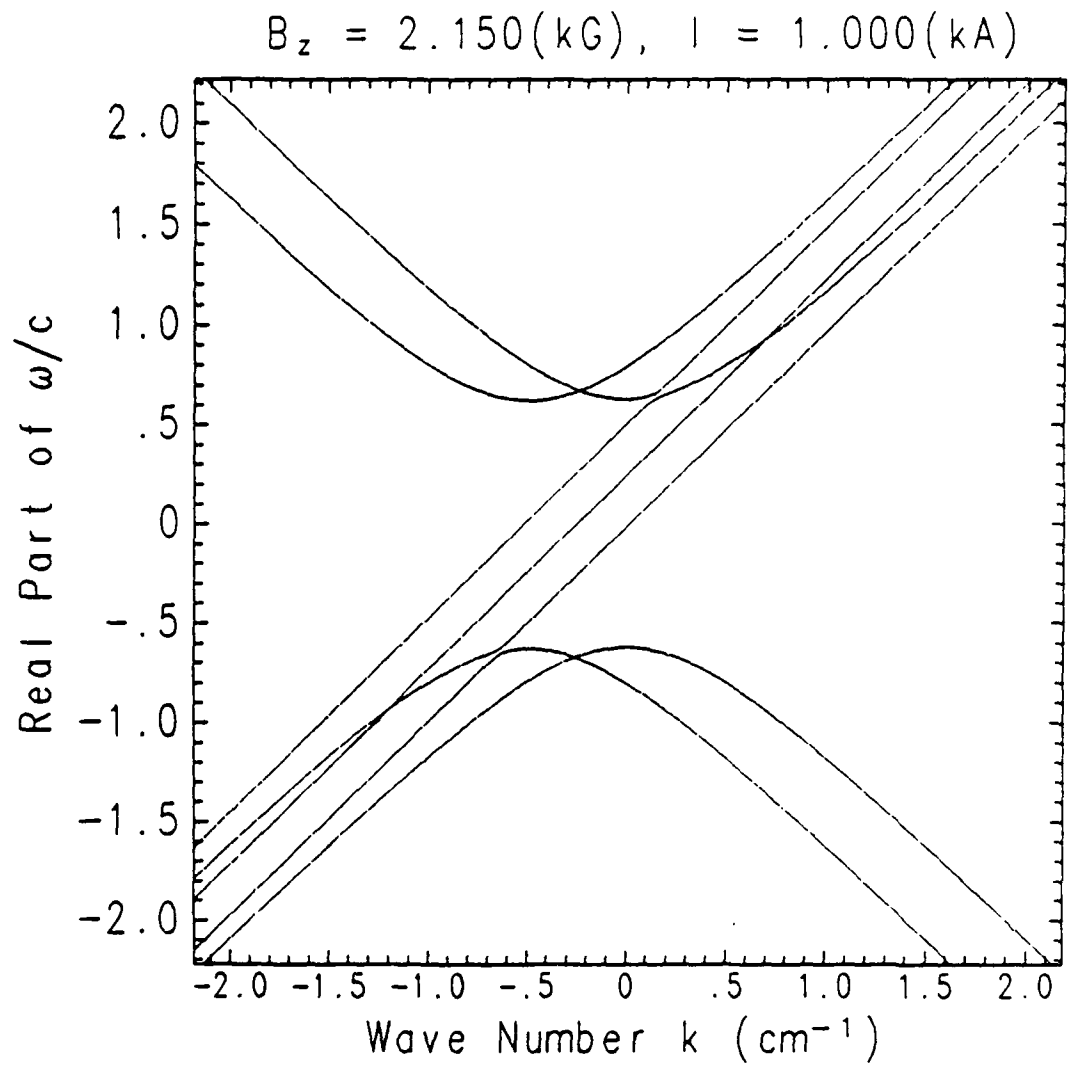


Fig. 4 (Continued) Dispersion diagram for the right-hand-circularly polarized waves for parameters in Table I with:

b) $B_o = 2.15 \text{ kG}$ ($K_o = 0.26 \text{ cm}^{-1}$) and $k_q = 0.5 \text{ cm}^{-1}$.

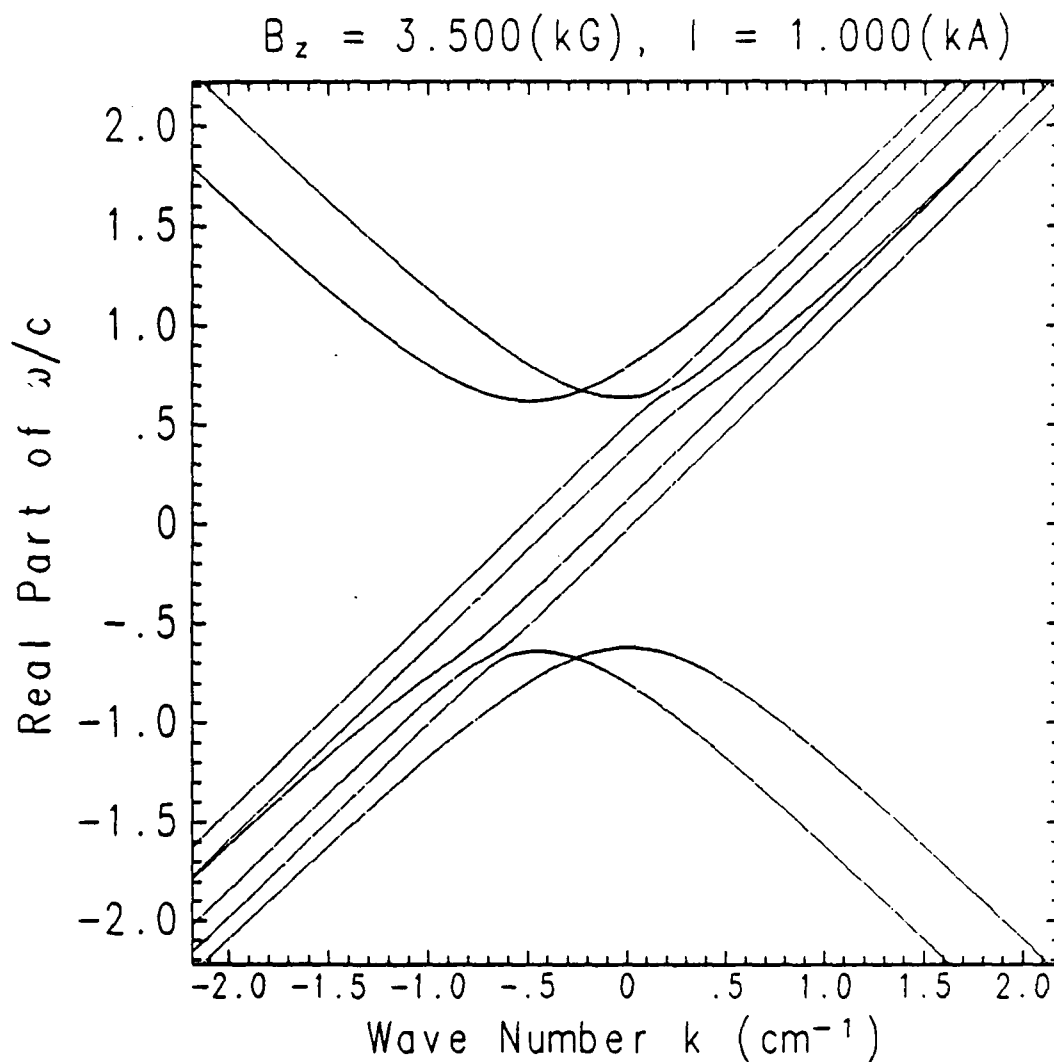


Fig. 4 (Continued) Dispersion diagram for the right-hand-circularly polarized waves for parameters in Table I with:

$$c) B_o = 3.5 \text{ kG } (K_o = 0.42 \text{ cm}^{-1}) \text{ and } k_q = 0.5 \text{ cm}^{-1}.$$

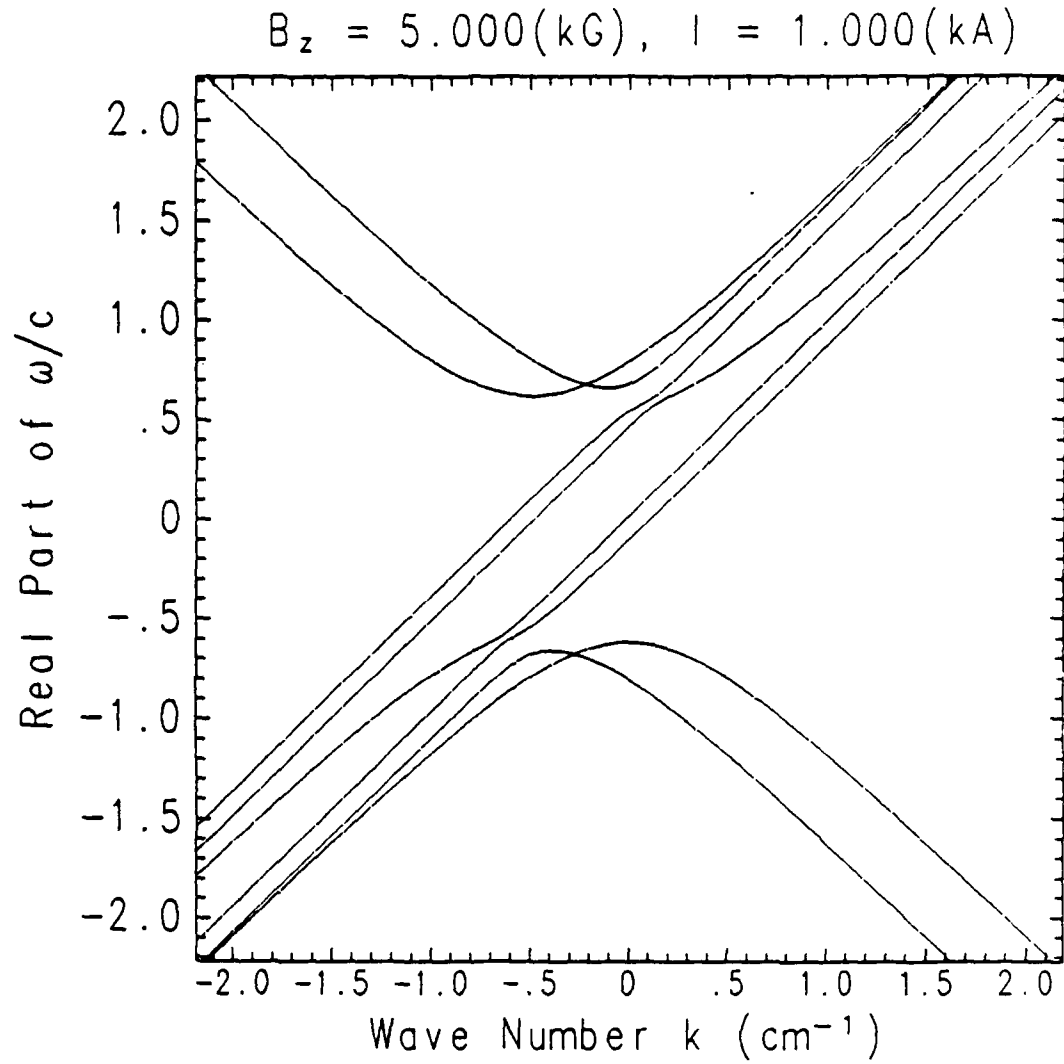


Fig. 4 (Continued) Dispersion diagram for the right-hand-circularly polarized waves for parameters in Table I with:

d) $B_o = 5.0 \text{ kG}$ ($K_o = 0.60 \text{ cm}^{-1}$) and $k_q = 0.5 \text{ cm}^{-1}$, and

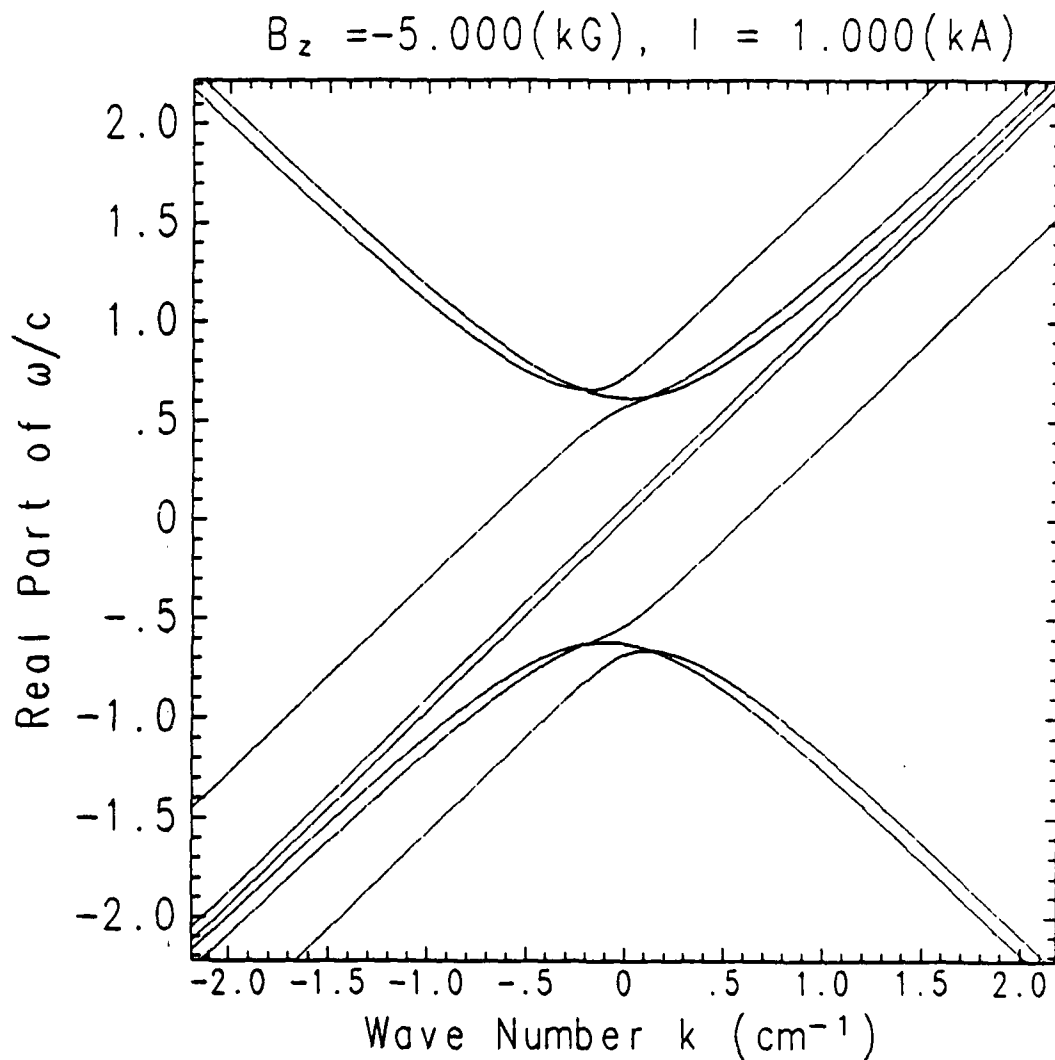


Fig. 4 (Continued) Dispersion diagram for the right-hand-circularly polarized waves for parameters in Table I with:

e) $B_o = -5.0 \text{ kG}$ ($K_o = -0.60 \text{ cm}^{-1}$) and $k_q = 0.1 \text{ cm}^{-1}$.

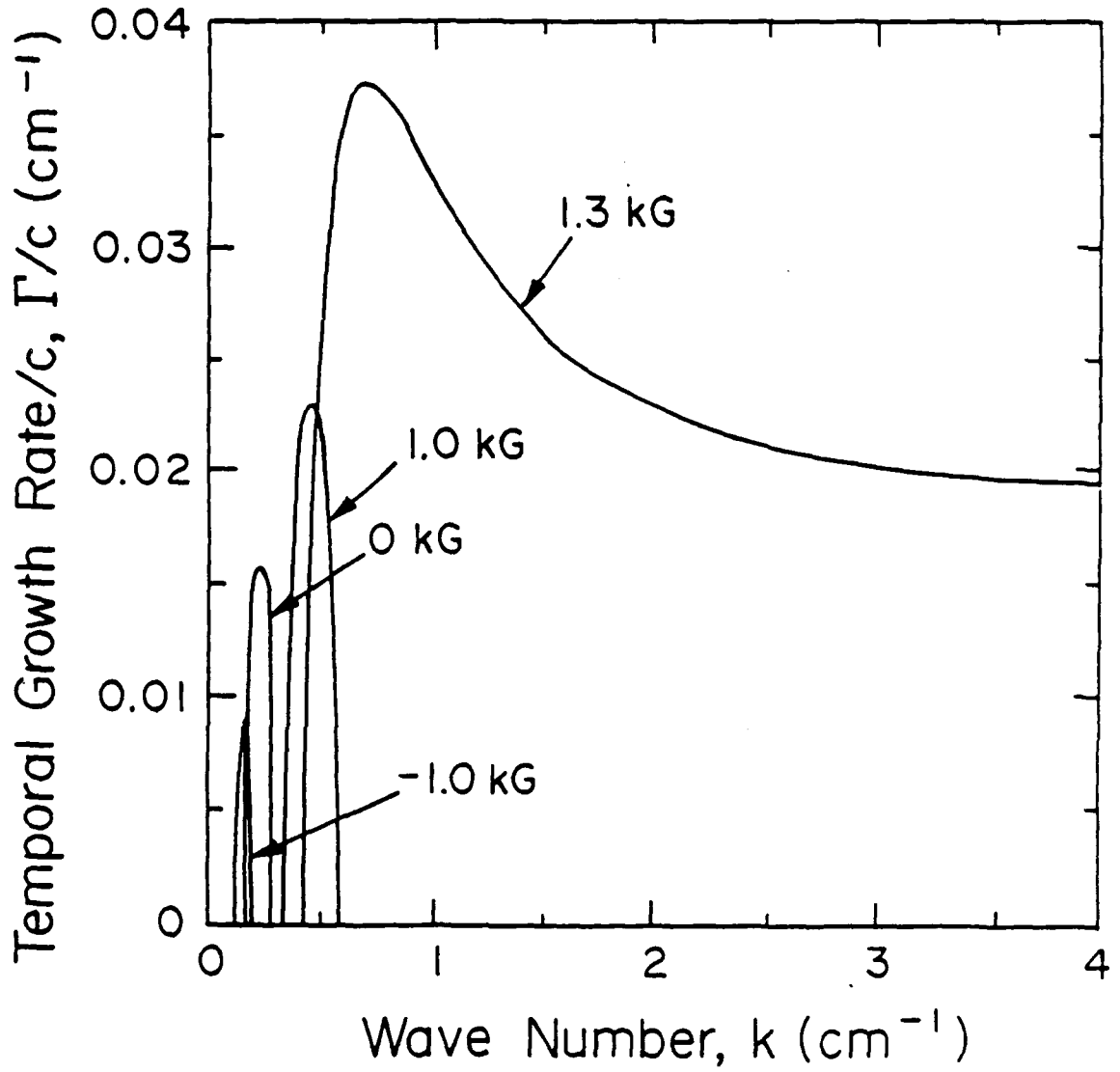


Fig. 5 Plots of the temporal growth rate versus k in three-wave unstable region I. for current

$I_b = 1 \text{ kA}$ and

- a) $B_o = -1.0 \text{ kG}$ ($K_o = -0.12 \text{ cm}^{-1}$),
- b) $B_o = 0$,
- c) $B_o = 1.0 \text{ kG}$ ($K_o = 0.12 \text{ cm}^{-1}$) and
- d) $B_o = 1.3 \text{ kG}$ ($K_o = 0.156 \text{ cm}^{-1}$).

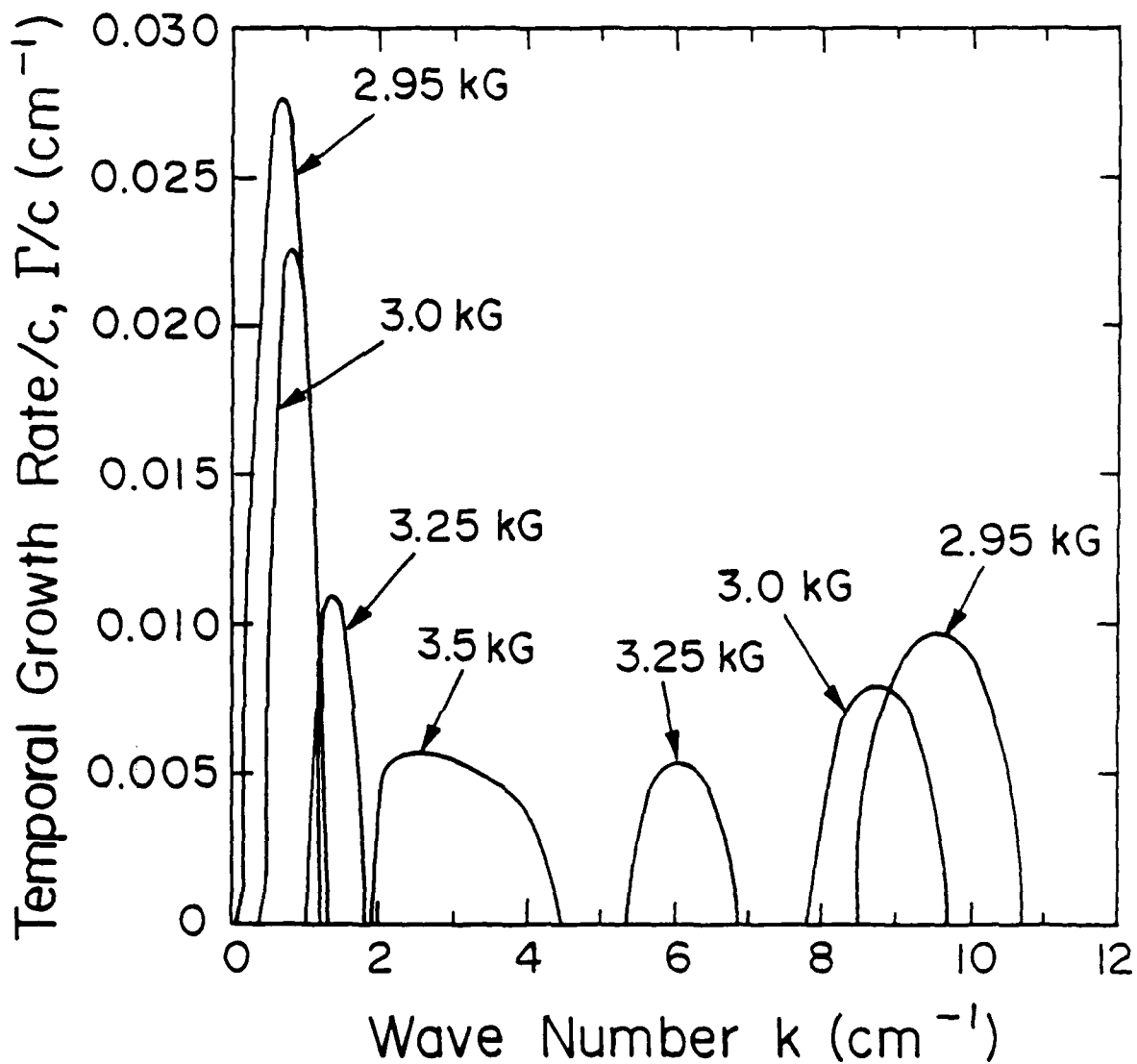


Fig. 6 Plots of the temporal growth rate versus k in the three-wave unstable region II, for current $I_b = 1 \text{ kA}$ and

- a) $B_o = 2.95 \text{ kG}$ ($K_o = 0.35 \text{ cm}^{-1}$),
- b) $B_o = 3.0 \text{ kG}$ ($K_o = 0.36 \text{ cm}^{-1}$),
- c) $B_o = 3.25 \text{ kG}$ ($K_o = 0.39 \text{ cm}^{-1}$) and
- d) $B_o = 3.5 \text{ kG}$ ($K_o = 0.41 \text{ cm}^{-1}$).

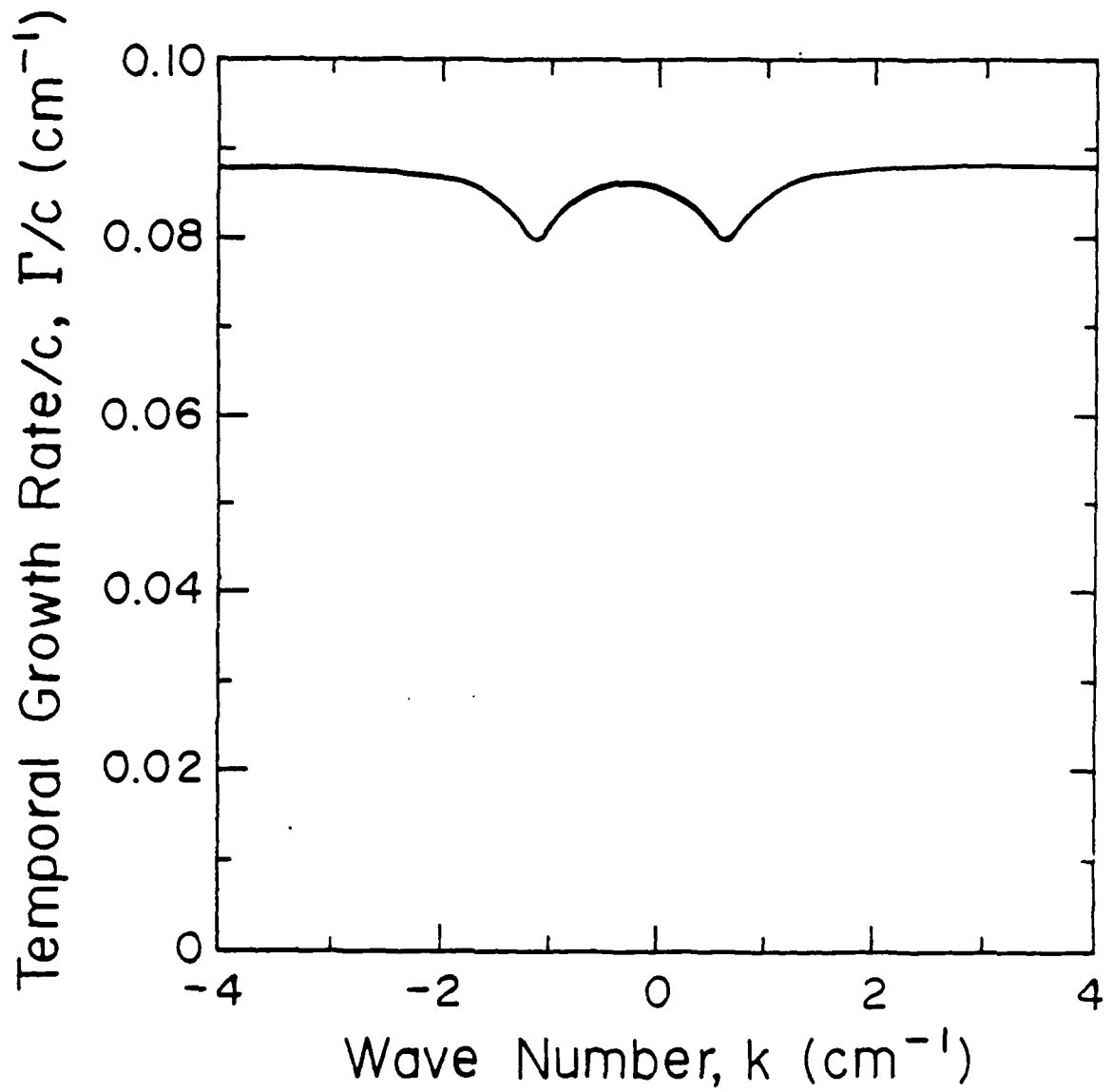


Fig. 7 A plot of the temporal growth rate versus k in the orbit unstable region, for current $I_b = 1 \text{ kA}$ and $B_o \approx 2.15 \text{ kG}$ ($K_o = 0.26 \text{ cm}^{-1}$).

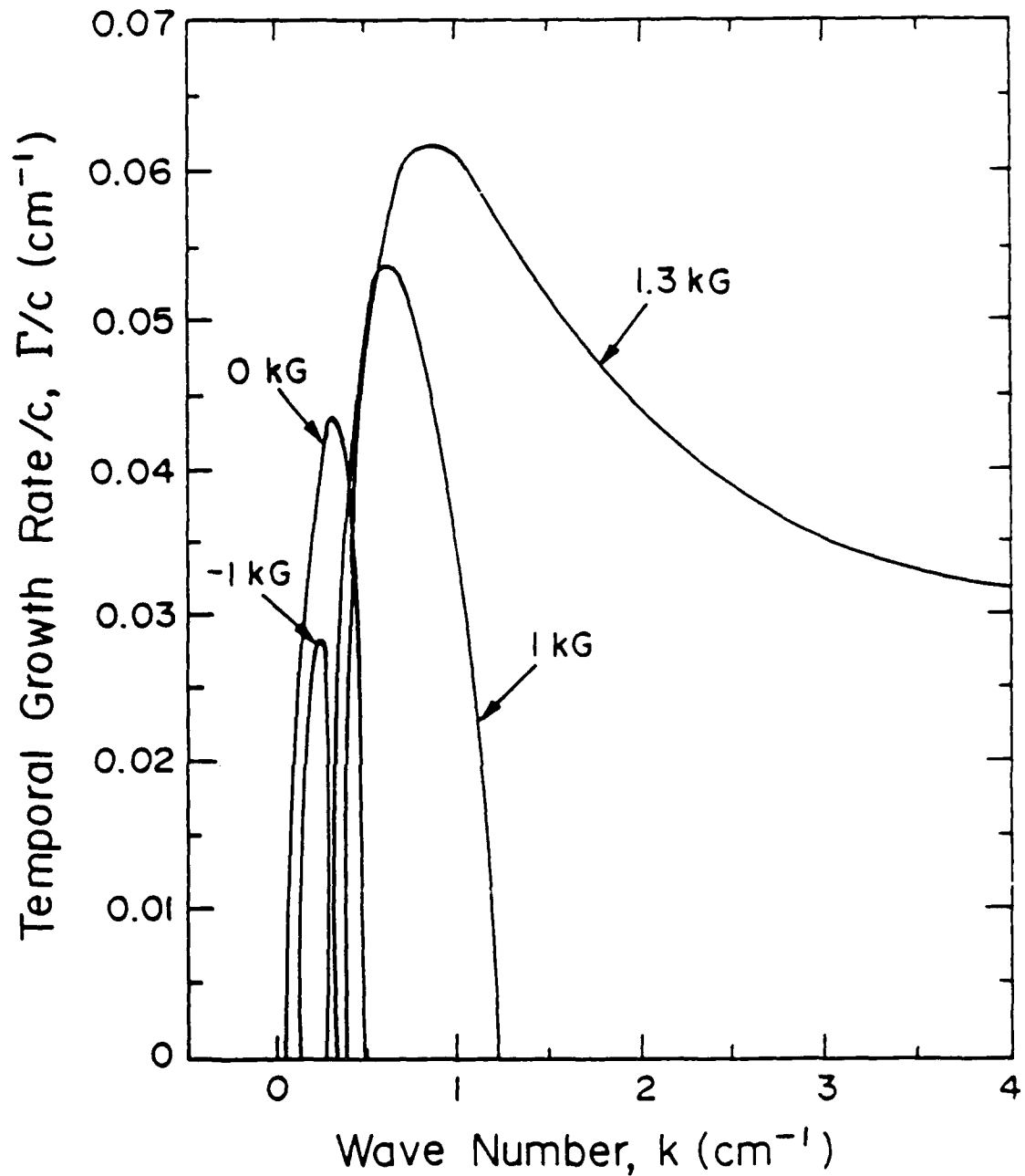


Fig. 8 Plots of the temporal growth rate versus k in three-wave unstable region I, for current

$I_b = 10 \text{ kA}$ and

- a) $B_o = -1.0 \text{ kG}$ ($K_o = -0.12 \text{ cm}^{-1}$),
- b) $B_o = 0$,
- c) $B_o = 1.0 \text{ kG}$ ($K_o = 0.12 \text{ cm}^{-1}$) and
- d) $B_o = 1.3 \text{ kG}$ ($K_o = 0.156 \text{ cm}^{-1}$).

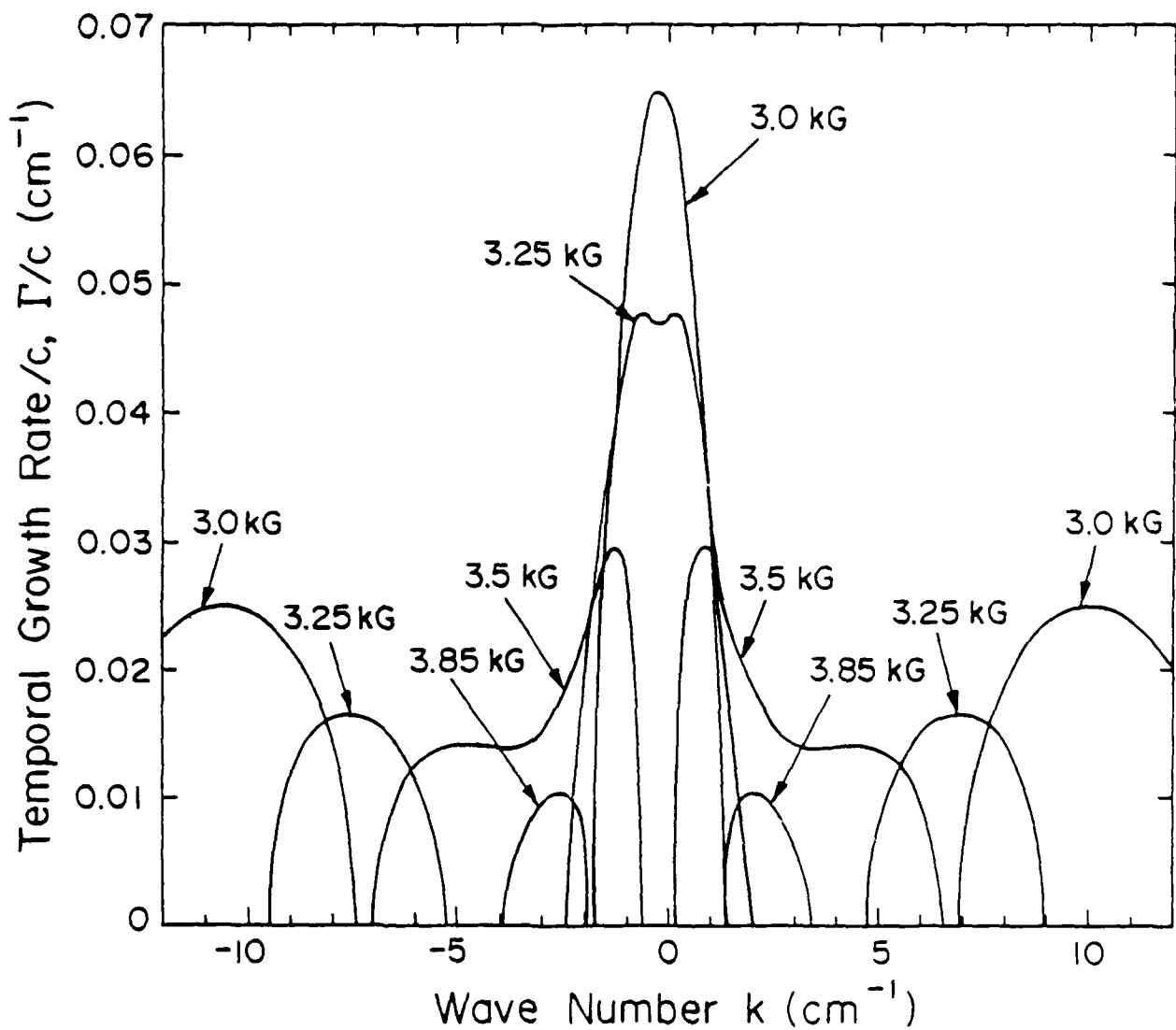


Fig. 9 Plots of the temporal growth rate versus k in the three-wave unstable region II, for current $I_b = 10 \text{ kA}$ and

- a) $B_o = 3.0 \text{ kG}$ ($K_o = 0.36 \text{ cm}^{-1}$),
- b) $B_o = 3.25 \text{ kG}$ ($K_o = 0.39 \text{ cm}^{-1}$),
- c) $B_o = 3.5 \text{ kG}$ ($K_o = 0.41 \text{ cm}^{-1}$) and
- d) $B_o = 3.85 \text{ kG}$ ($K_o = 0.45 \text{ cm}^{-1}$).

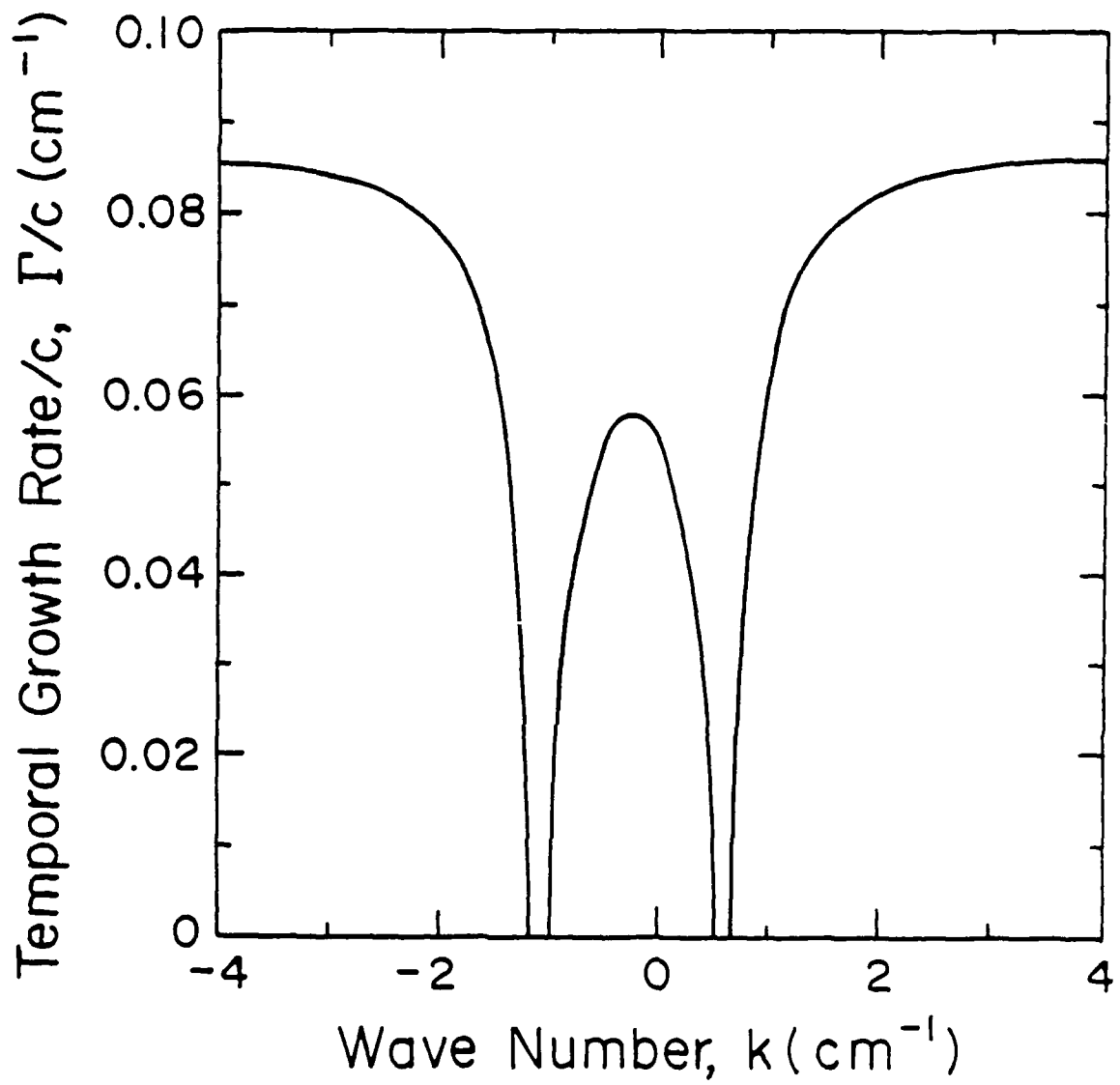


Fig. 10 A plot of the temporal growth rate versus k in the orbit unstable region, for current $I_b = 10 \text{ kA}$ and $B_o = 2.15 \text{ kG}$ ($K_o = 0.26 \text{ cm}^{-1}$).

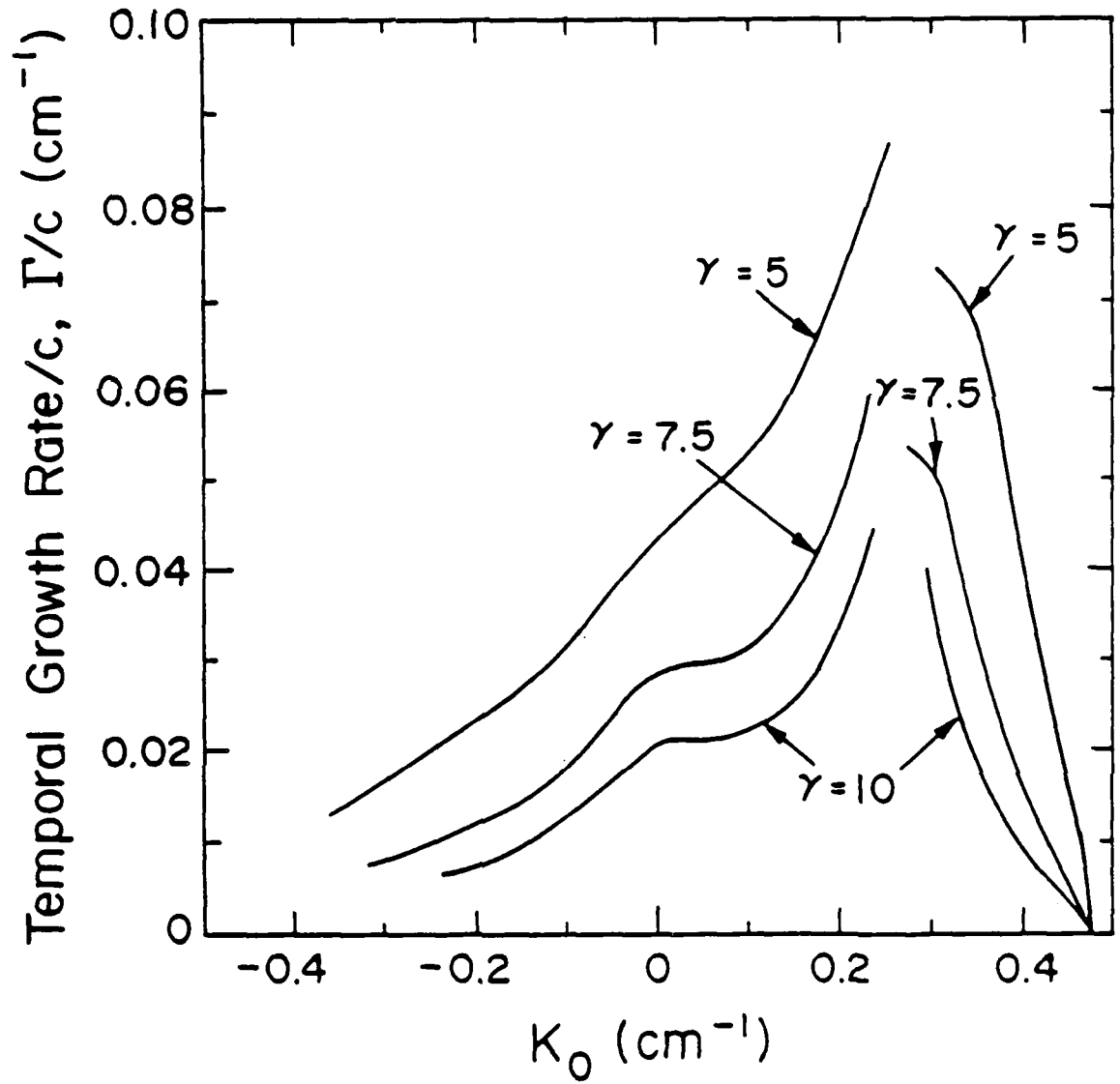


Fig. 11 Peak values of the temporal growth rate as a function of normalized guide field K_0 for $\gamma = 5, 7.5$ and 10 with current $I_b = 10 \text{ kA}$.

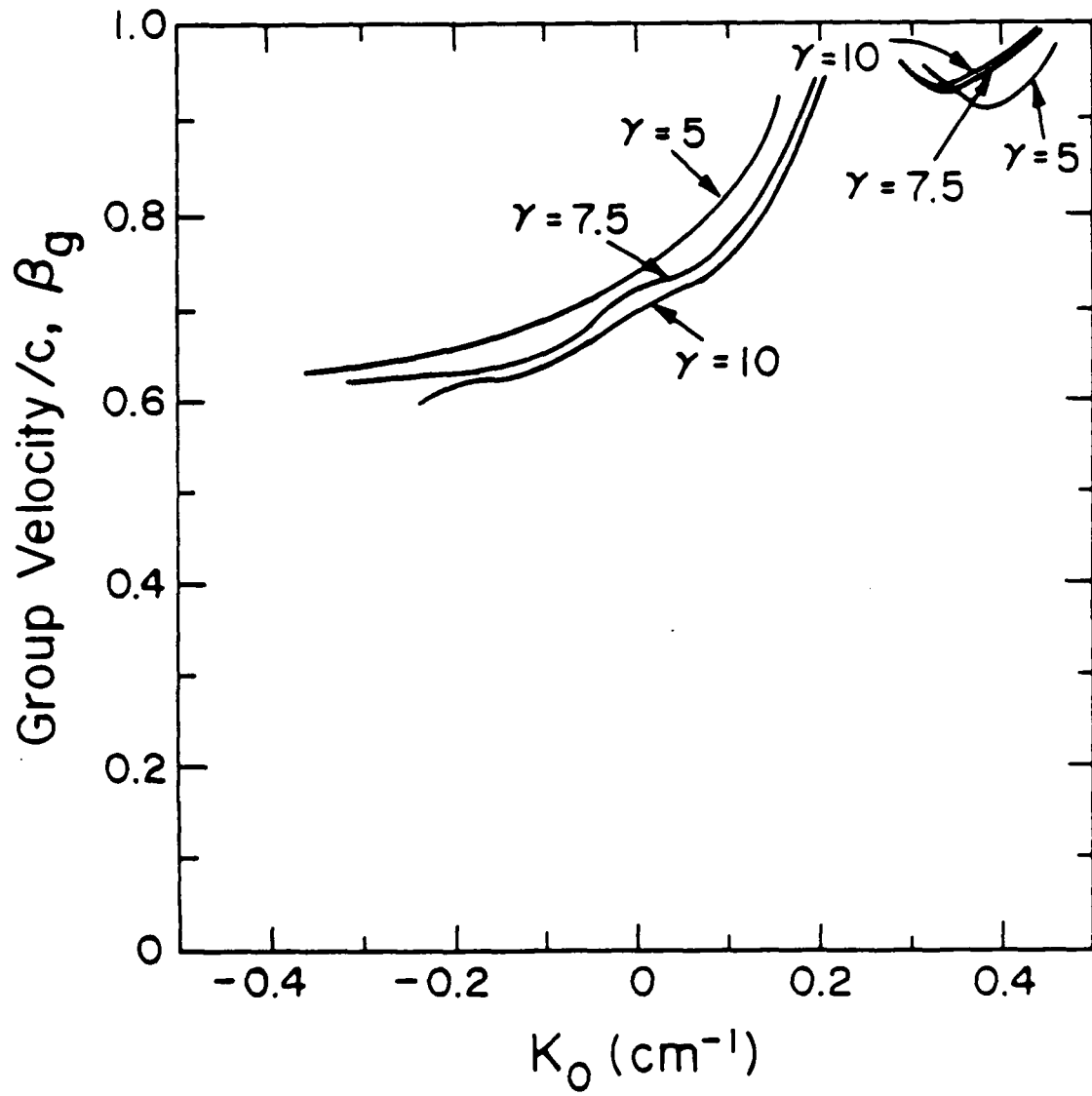


Fig. 12 Plots of group velocity as a function of K_0 for $\gamma = 5, 7.5$ and 10 with current $I_b = 10 \text{ kA}$.

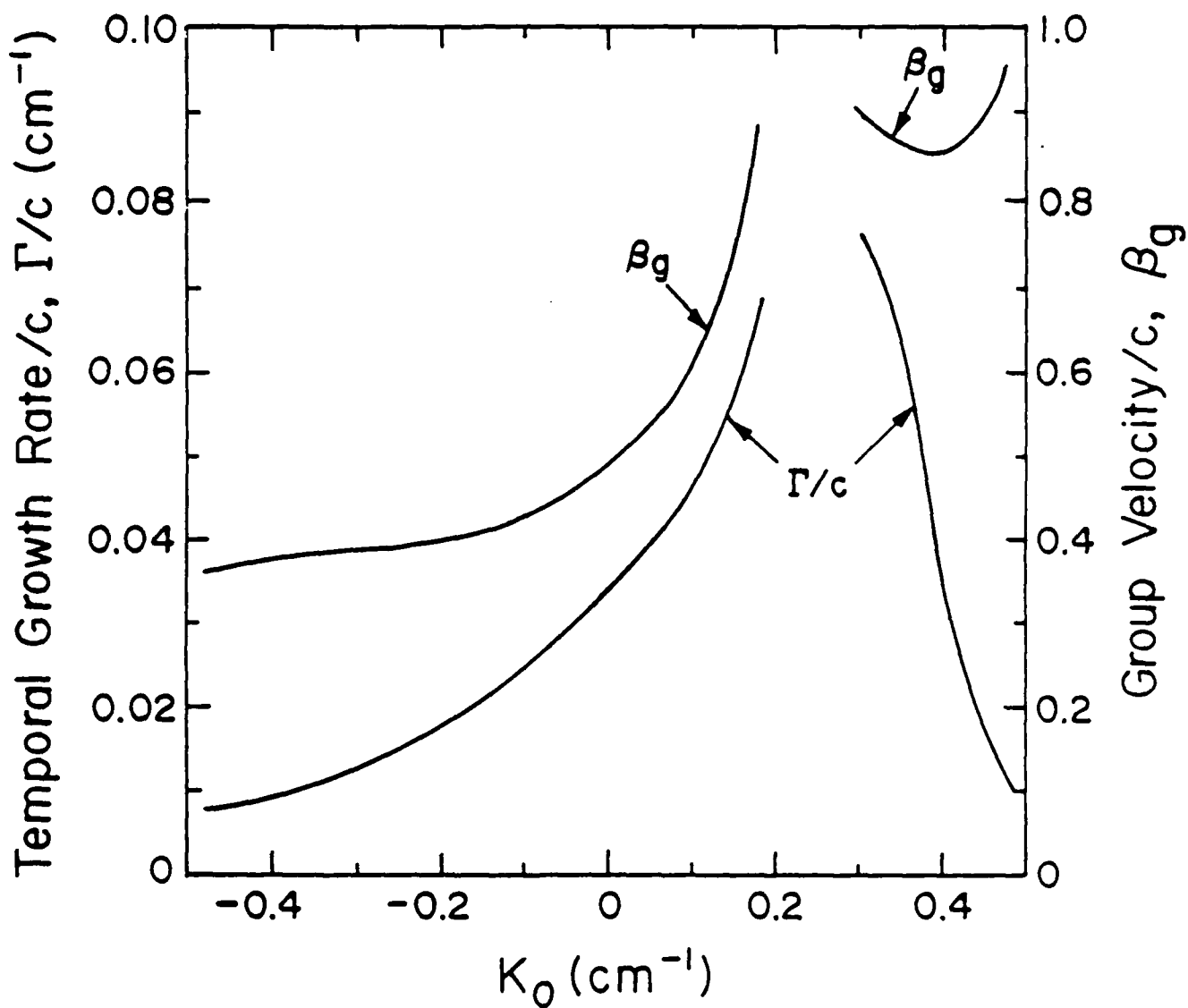


Fig. 13 Plots of the temporal growth rate and the group velocity as a function of K_0 for $r_g = 5 \text{ cm}$ and current $I_b = 10 \text{ kA}$, while keeping. Other parameters are the same as in Table I.

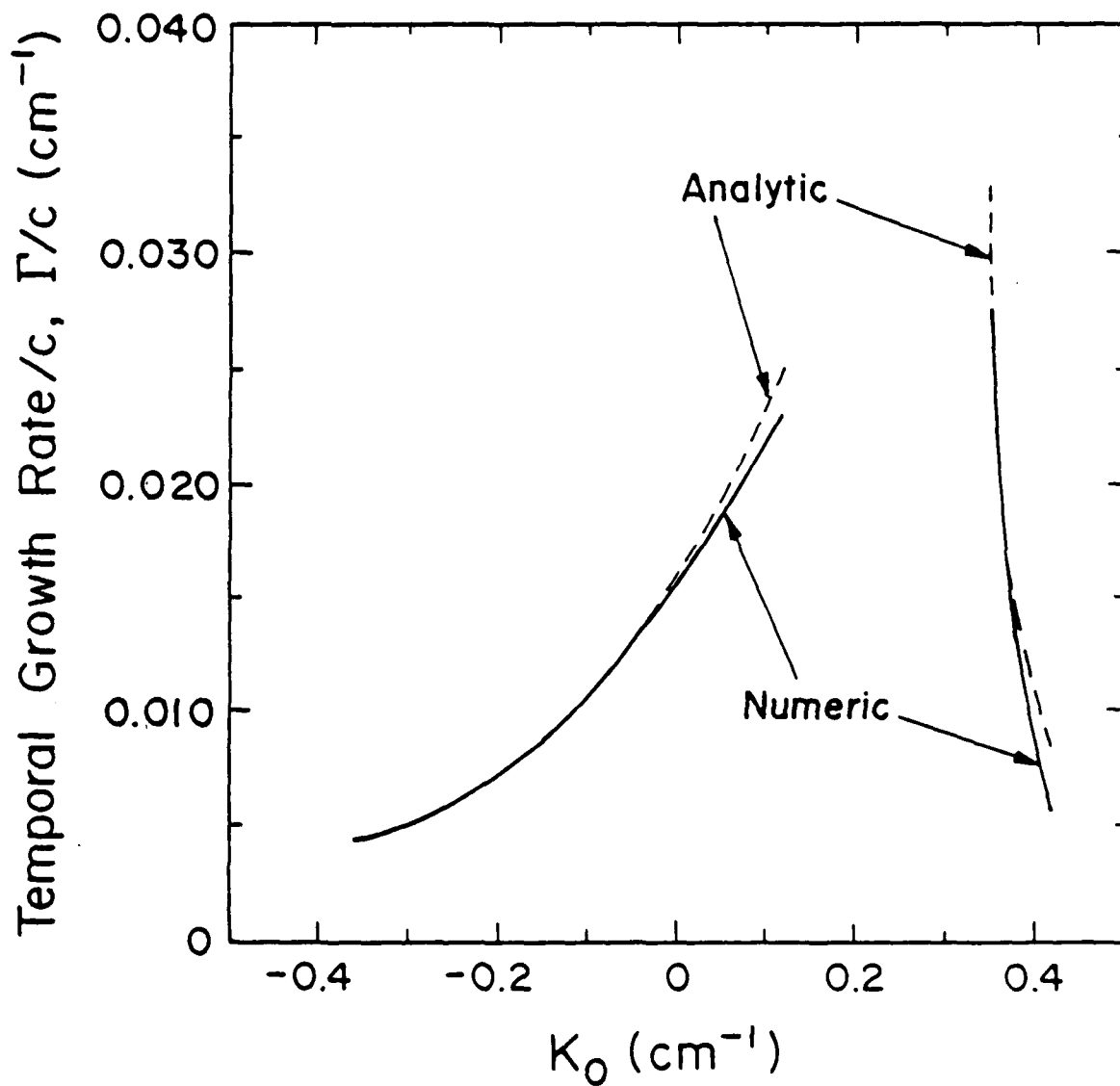


Fig. 14 Comparison of the maximum temporal growth rate as a function of K_0 for the values obtained from the numerically solved full dispersion relation (solid curves) and from the analytical expressions (dashed curves) for the parameters in Table I with current $I_b = 1$ kA.

Distribution List*

Naval Research Laboratory
4555 Overlook Avenue, S.W.

Attn: CAPT J. J. Donegan, Jr. - Code 1000
Dr. M. Lampe - Code 4792 (20 copies)
Dr. T. Coffey - Code 1001
Head, Office of Management & Admin - Code 1005
Deputy Head, Office of Management & Admin - Code 1005.1
Directives Staff, Office of Management & Admin - Code 1005.6
Director of Technical Services - Code 2000
ONR - Code 01Z4
NRL Historian - Code 2604
Dr. W. Ellis - Code 4000
Dr. J. Boris - Code 4040
Dr. M. Picone - Code 4040
Dr. M. Rosen - Code 4650
Dr. M. Haftel - Code 4665
Dr. S. Ossakow - Code 4700 (26 copies)
Dr. A. Robson - Code 4708
Dr. M. Friedman - Code 4750
Dr. R. Meger - Code 4750
Dr. J. Antoniadis - Code 4751
Dr. T. Peyser - Code 4751
Dr. D. Murphy - Code 4751
Dr. R. Pechacek - Code 4750.1
Dr. G. Cooperstein - Code 4770
Dr. A. Ali - Code 4780
Dr. D. Colombant - Code 4790
Dr. R. Fernsler - Code 4790
Dr. S. Gold - Code 4790
Dr. I. Haber - Code 4790
Dr. R. F. Hubbard - Code 4790
Dr. G. Joyce - Code 4790
Dr. Y. Lau - Code 4790
Dr. S. P. Slinker - Code 4790
Dr. P. Sprangle - Code 4790 (25 copies)
Dr. R. Taylor - 4790
Dr. J. Krall - Code 4790 (25 copies)
B. Pitcher - Code 4790A (25 copies)
Code 4790 (20 copies)
Mr. P. Boris - SAIC (Code 4790)
Library - Code 2628 (22 copies)
D. Wilbanks - Code 2634
Code 1220
Dr. C. M. Tang (25 copies)

* Every name listed on distribution gets one copy except for those where extra copies are noted.

Air Force Office of Scientific Research
Physical and Geophysical Sciences
Bolling Air Force Base
Washington, DC 20332
Attn: Major Bruce Smith

Air Force Weapons Laboratory
Kirtland Air Force Base
Albuquerque, NM 87117-6008
Attn: W. Baker (AFWL/NTYP)
D. Dietz (AFWL/NTYP)
R. W. Lemke
B. Godfrey

U. S. Army Ballistics Research Laboratory
Aberdeen Proving Ground, Maryland 21005
Attn: Dr. Donald Eccleshall (DRXBR-BM)
Dr. Anand Prakash
Dr. Clinton Hollandsworth

Avco Everett Research Laboratory
2385 Revere Beach Pkwy
Everett, Massachusetts 02149
Attn: Dr. R. Patrick
Dr. Dennis Reilly

Ballistic Missile Def. Ad. Tech. Ctr.
P.O. Box 1500
Huntsville, Alabama 35807
Attn: Dr. M. Havie (BMDSATC-1)

Chief of Naval Material
Office of Naval Technology
MAT-0712, Room 503
800 North Quincy Street
Arlington, VA 22217
Attn: Dr. Eli Zimet

Commander
Space and Naval Warfare Systems Command
National Center 1, Room 8E08
Washington, DC 20363-5100
Attn: RADM Robert L. Topping

Cornell University
369 Upson Hall
Ithaca, NY 14853
Attn: Prof. David Hammer

DASIAC - DETIR
Kaman Tempo
25600 Huntington Avenue, Suite 500
Alexandria, VA 22303
Attn: Mr. F. Wimeritz

Defense Advanced Research Projects Agen
1400 Wilson Blvd.
Arlington, VA 22209
Attn: Dr. H. L. Buchanan
Dr. B. Hui

Defense Nuclear Agency
Washington, DC 20305
Attn: Dr. Muhammad Owais (RAAE)

Department of Energy
Washington, DC 20545
Attn: Dr. Wilmot Hess (ER20:GTN,
High Energy and Nuclear Physics)
Mr. Gerald J. Peters (G-256)

Directed Technologies, Inc.
1500 Wilson Blvd. Suite 515
Arlington, VA 22209
Attn: Mr. Ira F. Kuhn
Dr. Nancy Chesser

C. S. Draper Laboratories
555 Technology Square
Cambridge, Massachusetts 02139
Attn: Dr. E. Olsson

General Dynamics Corporation
Pomana Division
1675 W. Mission Blvd.
P. O. Box 2507
Pomana, CA 92769-2507
Attn: Dr. Ken W. Hawko

Hy-Tech Research Corp.
P. O. Box 3422 FSS
Radford, VA 24143
Attn: Dr. Edward Yadowsky

HQ Foreign Technology Division
Wright-Patterson AFB, OH 45433
Attn: TUTD/Dr. C. Joseph Butler

Institute for Defense Analyses
1801 N. Beauregard Street
Alexandria, VA 22311
Attn: Dr. Deborah Levin
Ms. M. Smith

Intelcom Rad Tech.
P.O. Box 81087
San Diego, California 92138
Attn: Dr. W. Selph

JAYCOR
11011 Torreyana Road
P. O. Box 85154
San Diego, CA 92138-9259
Attn: Dr. Franklin S. Felber
Dr. Seung Kai Wong

JAYCOR
39650 Libery Street, Suite 320
Freemont, CA 94538
Attn: Dr. Kendal Casey

Joint Institute for Laboratory
Astrophysics
National Bureau of Standards and
University of Colorado
Boulder, CO 80309
Attn: Dr. Arthur V. Phelps

Kaman Sciences
1500 Garden of the Gods Road
Colorado Springs, CO 80933
Attn: Dr. John P. Jackson

Kaman Sciences
P. O. Drawer QQ
Santa Barbara, CA 93102
Attn: Dr. W. Hobbs

La Jolla Institute
P. O. Box 1434
La Jolla, CA 92038
Attn: Dr. K. Brueckner

Lawrence Berkeley Laboratory
University of California
Berkeley, CA 94720
Attn: Dr. Edward P. Lee
Dr. Thomas Fessenden

Lawrence Livermore National Laboratory
University of California
Livermore, California 94550
Attn: Dr. Simon S. Yu
Dr. Frank Chambers
Dr. James W.-K. Mark, L-477
Dr. William Fawley
Dr. William Barletta
Dr. William Sharp
Dr. Daniel S. Prono
Dr. John K. Boyd
Dr. John Clark
Dr. George J. Caporaso
Dr. Donald Prosnitz
Dr. John Stewart
Dr. Y. P. Chong
Major Kenneth Dreyer
Dr. Hans Kruger
Dr. Thaddeus J. Orzechowski
Dr. Michael R. Teague
Mr. John T. Weir

Dr. James E. Leiss
13013 Chestnut Oak Drive
Gaithersburg, MD 20878

Lockheed Missiles and Space Co.
3251 Hanover St.
Bldg. 205, Dept 92-20
Palo Alto, CA 94304
Attn: Dr. John Siambis

Los Alamos National Laboratory
P.O. Box 1663
Los Alamos, NM 87545
Attn: Dr. L. Thode
Dr. H. Dogliani, MS-5000
Mr. R. Carlson, MS-P940
Dr. Carl Ekdahl, MS-D410
Dr. Joseph Mack
Dr. Melvin I. Buchwald
Dr. David C. Moir

Maxwell Laboratories Inc.
8888 Balboa Avenue
San Diego, CA 92123
Attn: Dr. Ken Whitham

McDonnell Douglas Research Laboratories
Dept. 223, Bldg. 33, Level 45
Box 516
St. Louis, MO 63166
Attn: Dr. Carl Leader
Dr. Frank Bieniosek
Dr. John Honig

Mission Research Corporation
1720 Randolph Road, S.E.
Albuquerque, NM 87106
Attn: Dr. Thomas Hughes
Dr. Lawrence Wright
Dr. Kenneth Struve
Dr. Michael Mostrom
Dr. Dale Welch

Mission Research Corporation
P. O. Drawer 719
Santa Barbara, California 93102
Attn: Dr. C. Longmire
Dr. N. Carron

National Bureau of Standards
Gaithersburg, Maryland 20760
Attn: Dr. Mark Wilson

Naval Postgraduate School
Physics Department (Code 61)
Monterey, CA 93940
Attn: Prof. John R. Neighbours
Prof. Fred Buskirk
Prof. Kai Woehler
Prof. Xavier Maruyama

Naval Surface Warfare Center
White Oak Laboratory
Code R-41
Silver Spring, Maryland 20903-5000
Attn: Mr. V. M. Hinckley
Dr. M. H. Cha
Dr. H. S. Uhm
Dr. R. Fiorito
Dr. K. T. Nguyen
Dr. R. Stark
Dr. H. C. Chen
Dr. D. Rule
Dr. Matt Brown
Mrs. Carolyn Fisher (G42)
Dr. Eugene E. Nolting (H23)

Office of Naval Research
800 North Quincy Street
Arlington, VA 22217
Attn: Dr. C. W. Roberson
Dr. F. Saalfeld

Office of Naval Research (2 copies)
Department of the Navy
Code 01231C
Arlington, VA 22217

Office of Under Secretary of Defense
Research and Engineering
Room 3E1034
The Pentagon
Washington, DC 20301
Attn: Dr. John MacCallum

Physics International, Inc.
2700 Merced Street
San Leandro, CA. 94577
Attn: Dr. E. Goldman
Dr. James Benford
Dr. George B. Frazier
Mr. Ralph Genuario

Princeton University
Plasma Physics Laboratory
Princeton, NJ 08540
Attn: Dr. Francis Perkins, Jr.

Pulse Sciences, Inc.
600 McCormack Street
San Leandro, CA 94577
Attn: Dr. Sidney Putnam

Pulse Sciences, Inc.
2001 Wilshire Boulevard
Suite 600
Santa Monica, CA 90403
Attn: Dr. John R. Bayless
Dr. R. Adler

The Rand Corporation
2100 M Street, NW
Washington, DC 20037
Attn: Dr. Nikita Wells
Mr. Simon Kassel

Sandia National Laboratory
Albuquerque, NM 87115
Attn: Dr. David Hasti/1272
Dr. Collins Clark
Dr. John Freeman/1241
Dr. Charles Frost
Dr. George Kamin/1274
Dr. Gordon T. Leifeste
Dr. Gerald N. Hays
Dr. Michael G. Mazarakis/1272
Dr. John Wagner/1241
Dr. Ron Lipinski/1274
Dr. James Poukey
Dr. Milton J. Clauser/1261
Dr. Kenneth R. Prestvich/1240
Dr. Kevin O'Brien
Dr. Isaac R. Shokair
Dr. J. Pace VanDevender/1200

Science Applications Intl. Corp.
5150 El Camino Road
Los Altos, CA 94022
Attn: Dr. R. R. Johnston
Dr. Leon Feinstein
Dr. Douglas Keeley
Dr. E. Roland Parkinson

Science Applications Intl. Corp.
1710 Goodridge Drive
McLean, VA 22102
Attn: Mr. W. Chadsey
Dr. A Drobot
Dr. K. Papadopoulos
Dr. William W. Rienstra
Dr. Alan J. Toepfer
Dr. Alfred Mondelli
Dr. D. Chernin
Dr. R. Tsang

Science Research Laboratory, Inc.
1600 Wilson Boulevard
Suite 1200
Arlington, VA 22209
Attn: Dr. Joseph Mangano
Dr. Daniel Birx

Commander
Space & Naval Warfare Systems Command
PMW-145
Washington, DC 20363-5100
Attn: CAPT J. D. Fontana
LT Fritchie

SRI International
PSO-15
Molecular Physics Laboratory
333 Ravenswood Avenue
Menlo Park, CA 94025
Attn: Dr. Donald Eckstrom
Dr. Kenneth R. Stalder

Strategic Defense Initiative Org.
SDIO/T/DEO
The Pentagon
Washington, DC 20009-7100
Attn: Lt Col R. L. Gullickson
Dr. D. Duston

Titan/Spectron, Inc.
P. O. Box 4399
Albuquerque, NM 87196
Attn: Dr. R. Bruce Miller
Dr. John Smith

Titan Systems, Inc.
2685 Marine Way
Suite 1408
Mountain View, CA 94043
Attn: Dr. Kenneth W. Billman

Titan Systems, Inc.
9191 Towne Centre Dr.-Suite 500
San Diego, CA 92122
Attn: Dr. R. M. Dove

University of California
Physics Department
Irvine, CA 92664
Attn: Dr. Gregory Benford
Dr. Norman Rostoker

University of California
San Diego, CA 92110
Attn: Dr. Marshall N. Rosenbluth

University of Maryland
Physics Department
College Park, MD 20742
Attn: Dr. Y. C. Lee
Dr. C. Grebogi
Dr. W. Destler
Dr. C. Striffler

University of Michigan
Dept. of Nuclear Engineering
Ann Arbor, MI 48109
Attn: Prof. Terry Kammash
Prof. R. Gilgenbach

Director of Research
U.S. Naval Academy
Annapolis, MD 21402 (2 copies)

Do NOT make labels
for these two--below:
Records---(1 copy)

Naval Research Laboratory
Washington, DC 20375-5000
Code 2630
Timothy Calderwood